

# The Color Glass Condensate

FRANÇOIS GELIS, EDMOND IANCU

*IPhT, CEA/Saclay, 91191 Gif sur Yvette cedex, France*

*francois.gelis@cea.fr, edmond.iancu@cea.fr*

JAMAL JALILIAN-MARIAN

*Department of Natural Sciences, Baruch College, 17 Lexington Ave*

*New York, NY-10010, USA*

*CUNY Graduate Center, 365 fifth Ave, New York, NY-10016, USA*

*jamal.jalilian-marian@baruch.cuny.edu*

RAJU VENUGOPALAN

*Physics Department, BNL, Upton NY-11973, USA*

*raju@bnl.gov*

**Key Words** Quantum Chromodynamics, Saturation, Deep Inelastic Scattering  
Glasma, Multi-particle Production  
Quark Gluon Plasma, Heavy Ion Collisions

**Abstract** We provide a broad overview of the theoretical status and phenomenological applications of the Color Glass Condensate effective field theory describing universal properties of saturated gluons in hadron wavefunctions that are extracted from deeply inelastic scattering and hadron-hadron collision experiments at high energies.

CONTENTS

High energy QCD and the Color Glass Condensate . . . . .	3
Color Glass Condensate: theoretical status . . . . .	7
<i>Parton evolution at high energy</i> . . . . .	8
<i>Generic features of gluon saturation</i> . . . . .	11
<i>The Color Glass Condensate</i> . . . . .	12
<i>Advanced Theory topics</i> . . . . .	15
Collisions in the CGC framework . . . . .	16
<i>The CGC and DIS at small <math>x</math></i> . . . . .	16
<i>The CGC in <math>p+A</math> collisions</i> . . . . .	18
<i>Shattering CGCs in <math>A+A</math> collisions</i> . . . . .	20
Phenomenological applications of the CGC . . . . .	22
<i>DIS in <math>e+p</math> and <math>e+A</math> collisions</i> . . . . .	23
<i>Particle multiplicities in <math>d+A</math> and <math>A+A</math> collisions</i> . . . . .	26
<i>Inclusive spectra in <math>d+A</math> and <math>A+A</math> collisions</i> . . . . .	28
<i>Two hadron correlations in <math>d+A</math> and <math>A+A</math> collisions</i> . . . . .	29
Outlook: LHC and future DIS colliders . . . . .	31

## 1 High energy QCD and the Color Glass Condensate

Only 5% of the mass of the universe is “bright matter”, but 99% of this visible matter is described by QCD, the theory of the strong interactions. QCD has been described as a nearly perfect theory, with the only parameters being the masses of the current quarks (1). The vast bulk of visible matter is therefore “emergent” phenomena arising from the rich dynamics of the QCD vacuum and the interactions of the fundamental quark and gluon constituents of QCD. Although we have enough information from a wide range of experimental data and from numerical lattice computations that QCD is the right theory of the strong interactions, outstanding questions remain about how a variety of striking phenomena arise in the theory. This is because the complexity of the theory also makes it very difficult to solve.

Our focus in this review is on high energy scattering in QCD. A traditional approach to these phenomena is to divide them into “hard” or “soft” scattering, corresponding respectively to large or small momentum exchanges in the scattering. In the former case, because of the “asymptotic freedom” of QCD, phenomena such as jets can be computed in a perturbative framework. In the latter case, because the momentum transfer is small, the “infrared slavery” of QCD suggests that the coupling is large; the scattering therefore is intrinsically non-perturbative and therefore not amenable to first principles analysis. This is problematic because “soft” dynamics comprises the bulk of QCD cross-sections. In contrast, the perturbatively calculable hard cross-sections are rare processes<sup>1</sup>.

We shall argue here that the traditional separation of hard versus soft QCD dynamics is oversimplified because novel semi-hard scales generated dynamically at high energies allow one to understand highly non-perturbative phenomena in QCD using weak coupling methods. To clarify what we mean, consider inclusive cross-sections in deeply inelastic scattering (DIS) experiments of electrons off hadrons.

Inclusive cross-sections in DIS (see figure 1) can be expressed in terms of the Lorentz invariants i)  $x$  which corresponds, at lowest order in perturbation theory, to the longitudinal momentum fraction carried by a parton in the hadron, ii) the virtual photon four-momentum squared  $q^2 = -Q^2 < 0$  exchanged between the electron and the hadron, iii) the inelasticity  $y$ , the ratio of the photon energy to

---

<sup>1</sup>Lattice QCD is not of much help here because it is best suited to compute static properties of the theory.

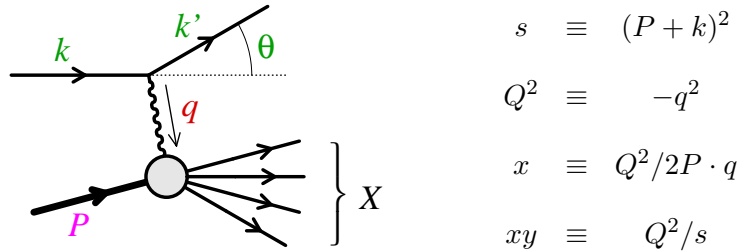


Figure 1: Kinematics of Deep Inelastic Scattering.

the electron energy in the hadron rest frame, and iv) the center of mass energy squared  $s$ . These satisfy the relation  $x = Q^2/sy$ . Instead of the dichotomy of “hard” versus “soft”, it is useful, for fixed  $y$ , to consider two asymptotic limits in DIS that better illustrate the QCD dynamics of high energy hadron wavefunctions. The first, called the Bjorken limit, corresponds to fixed  $x$  with  $Q^2, s \rightarrow \infty$ . The second is the Regge-Gribov limit of fixed  $Q^2, x \rightarrow 0$  and  $s \rightarrow \infty$ .

In the Bjorken limit of QCD, one obtains the parton model wherein the hadron is viewed, in the infinite momentum frame (IMF), as a dilute collection of valence quarks and “wee” (in the terminology coined by Feynman) partons—small  $x$  gluons and sea quark pairs. Albeit the number of wee partons is large at high energies, the hadron is dilute (as illustrated in figure 2) because the phase space density is very small for  $Q^2 \rightarrow \infty$ . In this limit, to leading order in the coupling constant, the interaction of a probe with the hadron, on the characteristic time scale  $1/Q$ , can be expressed as a hard interaction with an individual parton. In this “impulse approximation”, the interaction of the struck parton in the hadron with co-moving partons is suppressed due to time dilation. The separation of hard and soft scattering alluded to previously is valid here. Powerful tools such as the Operator Product Expansion (OPE) and factorization theorems extend, to high orders in the coupling constant expansion, the hard-soft separation between process-dependent physics at the scale  $1/Q$  and universal, long distance, non-perturbative Parton Distribution Functions (PDFs). The evolution of the separation of hard and soft scales is given by renormalization group (RG) equations called the DGLAP (Dokshitzer-Gribov-Lipatov-Altarelli-Parisi) equations (2).

The study of strong interactions in the Regge-Gribov limit predates QCD, and underlies concepts such as soft Pomeron and Reggeon exchanges, whose dynamics, described by “Reggeon Field Theory” (RFT), was believed to encompass much of the phenomena of multi-particle production. Albeit phenomenologically

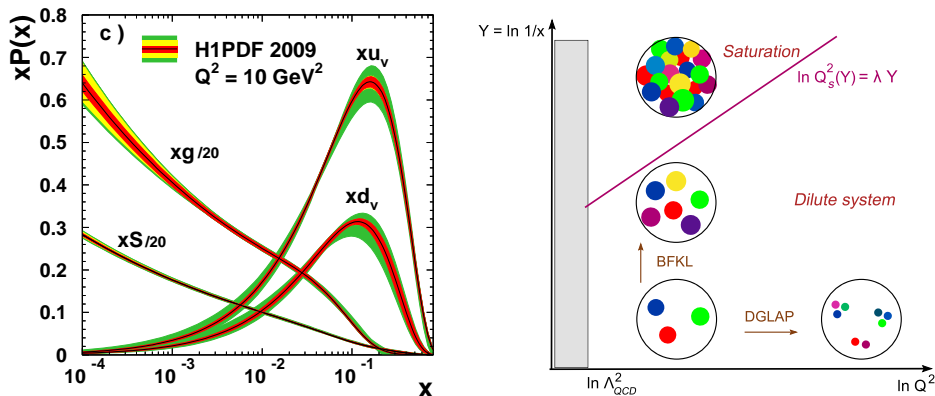


Figure 2: *Left: the  $x$ -evolution of the gluon, sea quark, and valence quark distributions for  $Q^2 = 10 \text{ GeV}^2$  measured at HERA (3). Right: the “phase–diagram” for QCD evolution; each colored dot represents a parton with transverse area  $\delta S_{\perp} \sim 1/Q^2$  and longitudinal momentum  $k^+ = xP^+$ .*

very suggestive (4), the dynamics of RFT is intrinsically non-perturbative and therefore not easily amenable to systematic computations. With the advent of high energy colliders, hadron structure in the Regge-Gribov limit can be explored with  $Q^2 \geq 1 \text{ GeV}^2$ . As strikingly demonstrated by the HERA DIS data shown in figure 2, the gluon distribution  $xG(x, Q^2)$  in a proton rises very fast with decreasing  $x$  at large, fixed  $Q^2$  – roughly, as a power  $x^{-\lambda}$  with  $\lambda \simeq 0.3$ . In the IMF frame of the parton model,  $xG(x, Q^2)$  is the number of gluons with a transverse area  $\delta S_{\perp} \geq 1/Q^2$  and a fraction  $k^+/P^+ \sim x$  of the proton longitudinal momentum<sup>2</sup>. In the Regge-Gribov limit, the rapid rise of the gluon distribution at small  $x$  is given by the BFKL (Balitsky-Fadin-Kuraev-Lipatov) equation (5), which we will discuss at some length later.

The stability of the theory formulated in the IMF requires that gluons have a maximal occupation number of order  $1/\alpha_s$ . This bound is saturated for gluon modes with transverse momenta  $k_{\perp} \leq Q_s$ , where  $Q_s(x)$  is a semi-hard scale, the “saturation scale”, that grows as  $x$  decreases. In this novel “saturation” regime of QCD (6), illustrated in figure 2 (right panel), the proton becomes a dense many body system of gluons. In addition to the strong  $x$  dependence, the saturation scale  $Q_s$  has an  $A$  dependence because of the Lorentz contraction of the nuclear parton density in the probe rest frame. The dynamics of gluons in the saturation regime is non-perturbative as is typical of strongly correlated systems. However, in a fundamental departure from RFT, this dynamics can be

<sup>2</sup>The light cone co-ordinates are defined as  $k^{\pm} = (k^0 \pm k^3)/\sqrt{2}$ .

computed using weak coupling methods as a consequence of the large saturation scale dynamically generated by gluon interactions. Thus instead of the “hard” plus “soft” paradigm of the Bjorken limit, one has a powerful new paradigm in the Regge-Gribov limit to compute the bulk of previously considered intractable scattering dynamics in hadrons and nuclei.

The Color Glass Condensate (CGC) is the description of the properties of saturated gluons in the IMF in the Regge-Gribov limit. The effective degrees of freedom in this framework are color sources  $\rho$  at large  $x$  and gauge fields  $A^\mu$  at small  $x$ . At high energies, because of time dilation, the former are frozen color configurations on the natural time scales of the strong interactions and are distributed randomly from event to event. The latter are dynamical fields coupled to the static color sources. It is the stochastic nature of the sources, combined with the separation of time scales, that justify the “glass” appellation. The “condensate” designation comes from the fact that in the IMF, saturated gluons have large occupation numbers  $\mathcal{O}(1/\alpha_s)$ , with typical momenta peaked about a characteristic value  $k_\perp \sim Q_s$ . The dynamical features of the CGC are captured by the JIMWLK<sup>3</sup> renormalization group (RG) equation that describes how the statistical distribution  $W[\rho]$  of the fast sources at a given  $x$  scale evolves with decreasing  $x$ . The JIMWLK RG is Wilsonian in nature because weakly coupled fields integrated out at a given step in the evolution are interpreted as “induced color charges” that modify the statistical weight distribution.

The CGC framework is quite powerful because, given an initial non-perturbative distribution of sources at an initial scale  $x_0$ , it allows one to compute systematically  $n$ -point gluon correlation functions and their evolution with  $x$  order by order in perturbation theory. In analogy to parton distribution functions in the Bjorken limit, the distribution  $W[\rho]$  captures the properties of saturated gluons. Unlike PDFs however, which in the IMF are parton densities,  $W[\rho]$  carries much more information. Further, in contrast to the “twist” expansion of the Bjorken limit which becomes extremely cumbersome beyond the leading order in  $1/Q$ , the CGC framework includes all twist correlations. Like the PDFs, the  $W$ ’s are universal: the same distributions appear in computations of inclusive quantities in both lepton-nucleus and hadron-nucleus collisions.

The CGC is interesting in its own right in what it reveals about the collective dynamics of QCD at high parton densities. The CGC RG equations indicate that –at fixed impact parameter– a proton and a heavy nucleus become indis-

---

<sup>3</sup>JIMWLK  $\equiv$  Jalilian-Marian, Iancu, McLerran, Weigert, Leonidov, Kovner.

tinguishable at high energy; the physics of saturated gluons is universal and independent of the details of the fragmentation region. This universal dynamics has a correspondence with reaction–diffusion processes in statistical physics. In particular, it may lie in a “spin glass” universality class. Understanding the nature of color screening and “long range order” in this universal dynamics offers possibilities for progress in resolving fundamental QCD questions regarding properties such as confinement and chiral symmetry. A specific area of progress is in the mapping of the CGC degrees of freedom to the traditional language of Pomerons and the consequent prospects for understanding soft QCD dynamics. In nuclear collisions, CGC dynamics produces “Glasma” field configurations at early times: strong longitudinal chromo-electric and chromo-magnetic fields color screened on transverse distance scales  $1/Q_s$ . These generate long range rapidity correlations, “sphaleron-like” topological fluctuations characterized by large Chern-Simons charge, and instabilities analogous to those seen in QED plasmas.

The CGC framework is applicable to a wide variety of processes in e+p/A, p+A and A+A collisions. It provides an *ab initio* approach to study thermalization in heavy ion collisions and the initial conditions for the evolution of a thermalized Quark Gluon Plasma (QGP). The interaction of hard probes with the Glasma is little understood and is important for quantifying the transport properties of the QGP precursor. A further phenomenological application of the CGC is to the physics of ultra high energy cosmic rays (7).

There are several reviews that discuss various aspects of the CGC and its applications in depth (8–10). Our aim here is to provide a broad pedagogical overview of the current status of theory and phenomenology for non-experts. The next section will focus on the theoretical status, while section 3 discusses the CGC in the context of DIS, hadronic and nuclear collisions. Section 4 presents the experimental results that probe the dynamics of saturated gluons. We will end this review with a brief outlook.

## 2 Color Glass Condensate: theoretical status

We will begin this section with an elementary discussion of QCD bremsstrahlung in the Regge-Gribov limit and use this discussion to motivate the BFKL equation, how it leads to gluon saturation and describe key features of saturation. The theoretical status of the CGC effective theory is then presented. The section ends with a discussion of some advanced topics that highlight open issues.

## 2.1 Parton evolution at high energy

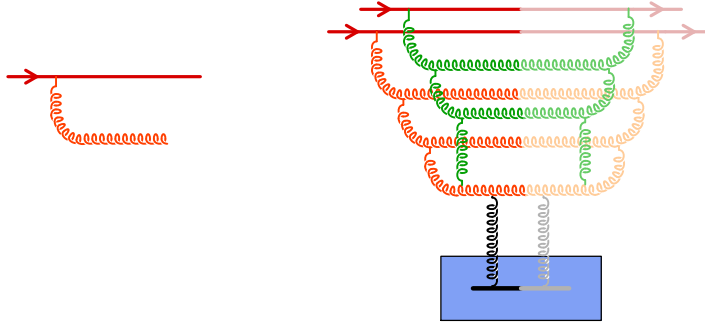


Figure 3: *Left: elementary bremsstrahlung radiation. Right: high energy scattering with evolution and recombination.*

The structure of a hadron depends upon the scales resolved by an external probe. Quantum fields bound within the hadron can radiate other virtual quanta which, by the uncertainty principle, live only for a short period of time. Therefore, what looks like an isolated quantum at a given resolution scale reveals a complicated substructure when probed with finer space–time resolution. The structure of the hadron in the IMF is specified by the longitudinal ( $k^+$ ) and transverse ( $k_\perp$ ) momentum distributions of its quanta and by their correlations—the latter become increasingly important with increasing density.

In perturbative QCD, parton evolution proceeds via bremsstrahlung, which favors the emission of *soft* and *collinear* gluons. The left part of figure 3 illustrates this elementary radiation process. When  $x \ll 1$ , to lowest order in  $\alpha_s$ , the differential probability for this emission is given by

$$dP_{\text{Brem}} \simeq \frac{\alpha_s C_R}{\pi^2} \frac{d^2 k_\perp}{k_\perp^2} \frac{dx}{x}, \quad (1)$$

where  $C_R$  is the  $SU(N_c)$  Casimir in the color representation of the emitter—  $N_c$  for a gluon and  $(N_c^2 - 1)/2N_c$  for a quark. This formula demonstrates the collinear ( $k_\perp \rightarrow 0$ ) and soft ( $x \rightarrow 0$ ) singularities mentioned above, which produce a logarithmic enhancement of gluon emission at small  $k_\perp$  and/or  $x$ . If the emitter at small  $x$  were a quark instead a gluon, there would be no small  $x$  enhancement; while the collinear enhancement is present for either emitter. This asymmetry is due to the spin 1 nature of the gluon.

A high energy scattering such as the one illustrated in the right part of figure 3 probes the number of gluons with a given  $x$  and transverse momenta  $k_\perp \leq Q$ .



From eq. (1), the gluon number is

$$x \frac{dN_g}{dx}(Q^2) = \frac{\alpha_s C_R}{\pi} \int_{\Lambda_{\text{QCD}}^2}^{Q^2} \frac{dk_{\perp}^2}{k_{\perp}^2} = \frac{\alpha_s C_R}{\pi} \ln \left( \frac{Q^2}{\Lambda_{\text{QCD}}^2} \right), \quad (2)$$

where the cutoff  $\Lambda_{\text{QCD}}$  has been introduced as a crude way to account for confinement: when confined inside a hadron, a parton has a minimum virtuality of  $\mathcal{O}(\Lambda_{\text{QCD}}^2)$ .

In QCD, gluons can radiate softer gluons and thus rapidly multiply as illustrated in figure 3. Each subsequent emission is  $\alpha_s$  suppressed however when the final value of  $x$  is small, these corrections become large. For a cascade with  $n$  intermediate gluons strongly ordered in  $x$ , one obtains

$$\alpha_s^n \int_x^1 \frac{dx_n}{x_n} \int_{x_n}^1 \frac{dx_{n-1}}{x_{n-1}} \dots \int_{x_2}^1 \frac{dx_1}{x_1} = \frac{1}{n!} \left( \alpha_s \ln \frac{1}{x} \right)^n. \quad (3)$$

When  $\alpha_s \ln(1/x) \gtrsim 1$ , the correct result for the gluon distribution is obtained by summing contributions from all such ladders. The sum *exponentiates*, modifying eq. (2) into

$$x \frac{dN_g}{dx dk_{\perp}^2} \sim \frac{\alpha_s C_R}{\pi} \frac{1}{k_{\perp}^2} e^{\omega \alpha_s Y}, \quad Y \equiv \ln \frac{1}{x}, \quad (4)$$

where  $\omega$  is a number of order unity which is not fixed by this rough estimate. The variable  $Y$  is known as the *rapidity*.

To go beyond this simple power counting argument, one must treat more accurately the kinematics of the ladder diagrams and include the associated virtual corrections. The result is the previously mentioned *BFKL equation* for the  $Y$ -evolution of the unintegrated gluon distribution. The solution of this equation, which resums perturbative corrections  $(\alpha_s Y)^n$  to all orders, confirms the exponential increase in eq. (4), albeit with a  $k_{\perp}$ -dependent exponent and modifications to the  $k_{\perp}^{-2}$ -spectrum of the emitted gluons.

An important property of the BFKL ladder is *coherence in time*. Because the lifetime of a parton in the IMF,  $\Delta x^+ \sim k^+/k_{\perp}^2 \propto x$ , the “slow” gluons at the lower end of the cascade have a much shorter lifetime than the preceding “fast” gluons. Therefore, for the purposes of small  $x$  dynamics, fast gluons with  $x' \gg x$  act as *frozen color sources emitting gluons at the scale  $x$* . Because these sources may overlap in the transverse plane, their color charges add coherently, giving rise to a large color charge density. The *average* color charge density is zero by gauge symmetry but fluctuations in the color charge density are nonzero and increase rapidly with  $1/x$ .

These considerations are at the heart of the CGC reformulation of BFKL evolution. However, in contrast to the original BFKL formulation, the CGC formalism (11–15) includes *non-linear* effects which appear when the gluon density becomes large.

The quantity which controls gluon interactions in the IMF is their *occupation number*—the number of gluons of a given color per unit transverse phase-space and per unit rapidity,

$$n(Y, k_\perp, b_\perp) \equiv \frac{(2\pi)^3}{2(N_c^2 - 1)} \frac{dN_g}{dY d^2\mathbf{k}_\perp d^2\mathbf{b}_\perp}, \quad (5)$$

where the impact parameter  $\mathbf{b}_\perp$  is the gluon position in the transverse plane. If  $n \ll 1$ , the system is dilute and gluon interactions are negligible. When  $n \sim \mathcal{O}(1)$  gluons start overlapping, but their interactions are suppressed by  $\alpha_s \ll 1$ . The interaction strength becomes of order one when  $n \sim \mathcal{O}(1/\alpha_s)$ . It is then that non-linear effects become important leading to gluon saturation.

Gluon occupancy is further amplified if instead of a proton we consider a large nucleus with atomic number  $A \gg 1$ . The transverse area scales like  $A^{2/3}$ , and the gluon occupation number scales as  $A^{1/3}$ . Thus, for a large nucleus, saturation effects become important at larger values of  $x$  than for a proton.

To be more specific, let us discuss a simplified version of the non-linear evolution equation for the occupation number. Consider an elementary increment in rapidity:  $Y \rightarrow Y + dY$ . Each preexisting gluon in the hadron has a probability  $\alpha_s dY$  to emit an additional soft gluon – the average increase is  $dn \sim \alpha_s n dY$ . Further, the emission vertex is non-local in  $k_\perp$  because the transverse momentum of the parent gluon is shared among the two daughter gluons. At high-energies, this non-locality is well approximated as a *diffusion* in the logarithmic variable  $t \equiv \ln(k_\perp^2)$ . Finally, two preexisting gluons can merge and produce a single final gluon with rapidity  $Y + dY$ . This process is quadratic in  $\alpha_s n$  and leads to a negative term in the evolution equation. Adding up these three effects, one obtains the evolution equation

$$\frac{\partial n}{\partial Y} \simeq \omega \alpha_s n + \chi \alpha_s \partial_t^2 n - \beta \alpha_s^2 n^2, \quad (6)$$

where  $\omega$ ,  $\chi$ , and  $\beta$  are numbers of order unity. This equation mimics the BFKL equation (5) if one drops the term quadratic in  $\alpha_s n$  in the r.h.s., and mimics its non-linear extensions that include saturation if one keeps the quadratic term.

## 2.2 Generic features of gluon saturation

Although a toy model, eq. (6) captures essential features of saturation<sup>4</sup>. If  $\alpha_s n \ll 1$ , one can neglect the quadratic term, and eq. (6) predicts an exponential growth in  $Y$  of the gluon occupation number. But when  $\alpha_s n \sim 1$ , the negative non-linear term turns on and tames the growth. In fact, eq. (6) has a fixed point at  $n = \omega/(\beta\alpha_s)$  where its r.h.s. vanishes—the evolution stops when this value of  $n$  is reached, resulting in gluon saturation in the spirit of early works (6).

Eq. (6) also reveals the emergence of a transverse momentum scale  $Q_s(Y)$  that characterizes saturation. This scale is the  $k_\perp$  where gluon occupancy becomes of  $\mathcal{O}(1/\alpha_s)$ . As a function of transverse momentum, the occupation number  $n(Y, k_\perp)$  is  $\mathcal{O}(1/\alpha_s)$  if  $k_\perp \lesssim Q_s(Y)$ , and decreases rapidly above  $Q_s(Y)$  ( $n \propto 1/k_\perp^2$  for  $k_\perp \gg Q_s(Y)$ ). The shape of  $n(Y, k_\perp)$  as a function of  $k_\perp$  is known as the *saturation front*. Note that  $Q_s$ , the typical gluon transverse momentum at the rapidity  $Y$ , increases with energy and becomes a semi-hard scale ( $Q_s(Y) \gg \Lambda_{\text{QCD}}$ ) at sufficiently high energy.

Eq. (6) belongs to the generic class of *reaction-diffusion processes* (19). These are processes where an entity can hop to neighboring locations (diffusion term  $\chi\alpha_s\partial_t^2 n$ ), can split into two identical entities (the term  $\omega\alpha_s n$ ), and where two entities can merge into a single one (the term  $\beta\alpha_s^2 n^2$ ). In the limit of large occupation numbers, these processes admit the mean field description of eq. (6), which in the context of statistical physics is known as the *Fisher-Kolmogorov-Petrovsky-Piscounov (FKPP) equation* (19). In QCD, the closest equation of this type is the Balitsky-Kovchegov (BK) equation (13). The correspondence between the BK and FKPP equations, originally noticed in (20), clarifies the properties of saturation fronts in QCD in analogy with known properties of reaction–diffusion processes.

A crucial property is the emergence of *traveling waves*. The saturation front generated by this equation propagates without distortion at constant speed; one has  $n(Y, t) = n(t - \lambda_s Y)$  with  $\lambda_s$  a constant. This property has been verified

---

<sup>4</sup>Our discussion oversimplifies the mechanism for gluon saturation. In the saturation regime, gluons form configurations that screen their color charge over transverse scales  $\sim 1/Q_s$  (16,17). Thus, gluons with momentum  $k_\perp \lesssim Q_s$  are emitted from a quasi-neutral patch of color sources, and their occupation number grows only *linearly* in  $Y$  (16,18) – much slower than the exponential growth in the region  $k_\perp \gg Q_s$ .

in numerical studies of the BK equation (21, 22) and in analytic studies of the BFKL equation in the presence of a saturation boundary (23, 24). It provides a natural explanation of the *geometric scaling* phenomenon observed in the HERA data (25, 26) (see section 3.1). In QCD, a front moving with constant speed  $\lambda_s$  is equivalent to the saturation momentum increasing exponentially with  $Y$ ,

$$Q_s^2(Y) \simeq Q_0^2 e^{\lambda_s Y} \quad \text{with} \quad \lambda_s \approx 4.9 \alpha_s, \quad (7)$$

where  $Q_0$  is some non-perturbative initial scale. For a large nucleus,  $Q_0^2$  scales like  $A^{1/3}$  as does  $Q_s^2(Y)$  for any  $Y$ . This form of the saturation momentum is modified to  $Q_s^2 = Q_0^2 e^{\sqrt{\lambda(Y+Y_0)}}$  when the running of the strong coupling is taken into account; see (24) for a detailed study of higher order effects on the energy dependence of  $Q_s$ .

### 2.3 The Color Glass Condensate

The CGC is an *effective field theory (EFT)* based on the separation of the degrees of freedom into fast frozen color sources and slow dynamical color fields (11). A *renormalization group equation* –the JIMWLK equation (14, 15)– ensures the independence of physical quantities with respect to the cutoff that separates the two kinds of degrees of freedom.

The fast gluons with longitudinal momentum  $k^+ > \Lambda^+$  are frozen by Lorentz time dilation in configurations specified by a color current  $J_a^\mu \equiv \delta^{\mu+} \rho^a$ , where  $\rho^a(x^-, x_\perp)$  is the corresponding color charge density. On the other hand, slow gluons with  $k^+ < \Lambda^+$  are described by the usual gauge fields  $A^\mu$  of QCD. Because of the hierarchy in  $k^+$  between these two types of degrees of freedom, they are coupled eikonally by a term  $J_\mu A^\mu$ . The fast gluons thus act as sources for the fields that represent the slow gluons. Although it is frozen for the duration of a given collision, the color source density  $\rho^a$  varies randomly event by event. The CGC provides a gauge invariant distribution  $W_{\Lambda^+}[\rho]$ , which gives the probability of a configuration  $\rho$ . This functional encodes all the correlations of the color charge density at the cutoff scale  $\Lambda^+$  separating the fast and slow degrees of freedom. Given this statistical distribution, the expectation value of an operator at the scale  $\Lambda^+$  is given by

$$\langle \mathcal{O} \rangle_{\Lambda^+} \equiv \int [D\rho] W_{\Lambda^+}[\rho] \mathcal{O}[\rho], \quad (8)$$

where  $\mathcal{O}[\rho]$  is the expectation value of the operator for a particular configuration  $\rho$  of the color sources.

The power counting of the CGC EFT is such that in the saturated regime the sources  $\rho$  are of order  $g^{-1}$ . Attaching an additional source to a given Feynman graph does not alter its order in  $g$ ; the vertex where this new source attaches to the graph is compensated by the  $g^{-1}$  of the source. Thus, computing an observable at a certain order in  $g^2$  requires the resummation of all the contributions obtained by adding extra sources to the relevant graphs. The leading order in  $g^2$  is given by a sum of tree diagrams, which can be expressed in terms of classical solutions of the Yang-Mills equations. Moreover, for inclusive observables (27), these classical fields obey a simple boundary condition: they vanish when  $t \rightarrow -\infty$ .

Next-to-leading order (NLO) computations in the CGC EFT involve a sum of one-loop diagrams embedded in the above classical field. To prevent double counting, momenta in loops are required to be below the cutoff  $\Lambda^+$ . This leads to a logarithmic dependence in  $\Lambda^+$  of these loop corrections. These logarithms are large if  $\Lambda^+$  is well above the typical longitudinal momentum scale of the observable considered, and must be resummed.

For gluon correlations inside the hadron wavefunction and also for sufficiently inclusive observables in a collision, the leading logarithms are universal and can be absorbed into a redefinition of the distribution  $W_{\Lambda^+}[\rho]$  of the hard sources. The evolution of  $W_{\Lambda^+}[\rho]$  with  $\Lambda^+$  is governed by the functional JIMWLK equation

$$\frac{\partial W_{\Lambda^+}[\rho]}{\partial \ln(\Lambda^+)} = -\mathcal{H} \left[ \rho, \frac{\delta}{\delta \rho} \right] W_{\Lambda^+}[\rho], \quad (9)$$

where  $\mathcal{H}$  is known as the JIMWLK Hamiltonian. This operator contains up to two derivatives  $\partial/\partial\rho$ , and arbitrary powers in  $\rho$ . Its explicit expression can be found in refs. (8,14,15). The derivation of the JIMWLK equation will be sketched in the section 3.1.

Numerical studies of JIMWLK evolution were performed in (22,28). An analytic, albeit formal, solution to the JIMWLK equation was constructed in (29) in the form of a path integral. Alternatively, the evolution can be expressed as an infinite hierarchy of coupled non-linear equations for  $n$ -point Wilson line correlators—often called the Balitsky hierarchy (12). In this framework, the BK equation is a mean field approximation of the JIMWLK evolution, valid in the limit of a large number of colors  $N_c \rightarrow \infty$ . Numerical studies of the JIMWLK equation (22,28) have found only small differences with the BK equation.

Let us finally comment on the initial condition for the JIMWLK equation which is also important in understanding its derivation. The evolution should

start at some cutoff value in the longitudinal momentum scale  $\Lambda_0^+$  at which the saturation scale is already a (semi)hard scale, say  $Q_{s0} \gtrsim 1$  GeV, for perturbation theory to be applicable. The gluon distribution at the starting scale is in general non-perturbative and requires a model. A physically motivated model for the gluon distribution in a large nucleus is the McLerran-Venugopalan model (11). In a large nucleus, there is a window in rapidity where evolution effects are not large but  $x$  is still sufficiently small for a probe not to resolve the longitudinal extent of the nucleus. In this case, the probe “sees” a large number of color charges, proportional to  $A^{1/3}$ . These charges add up to form a higher dimensional representation of the gauge group, and can therefore be treated as classical color distributions (11,30). Further, the color charge distribution  $W_{\Lambda_0^+}[\rho]$  is a Gaussian distribution<sup>5</sup> in  $\rho$ . The variance of this distribution –the color charge squared per unit area– is proportional to  $A^{1/3}$  and provides a semi-hard scale that makes weak coupling computations feasible. In addition to its role in motivating the EFT and serving as the initial condition in JIMWLK evolution, the MV model allows for direct phenomenological studies in p+A and A+A collisions in regimes where the values of  $x$  are not so small as to require evolution.

The dynamics of small  $x$  gluons in QCD may be universal in more than one sense (33). A weak form of this universality is that their dynamics in both hadrons and nuclei is controlled only by the saturation scale with its particular dependence on energy and nuclear size. A stronger form of the universality is noticed in particular for the solution of the BK equation with running coupling effects; the saturation scale, for both hadrons and nuclei, at fixed impact parameter, becomes the same asymptotically with increasing energy (34). The strongest form of the universality is that the RG flows in the saturation regime have a fixed point corresponding to universal “critical” exponents describing the behavior of multiparton correlation functions. As discussed further below, the RG equations for high energy QCD lie in a wide class of reaction-diffusion processes which have universal properties remarkably close to those of spin glasses (35).

---

<sup>5</sup>There is a additional term, corresponding to the cubic Casimir; which is parametrically suppressed for large nuclei (31). This term generates Odderon excitations in the JIMWLK/BK evolution (32).

## 2.4 Advanced Theory topics

Reaction–diffusion processes exhibit an extreme sensitivity to *particle number fluctuations* (36–38), generated by gluon splittings, which produce correlations among pairs of gluons (39). This effect is of higher order in  $\alpha_s$ , and is linear in  $n$  since it results from the splitting of a single gluon. Conversely, producing two gluons without this splitting leads to a term that has one less power of  $\alpha_s$ , but of order  $n^2$ . Thus, the splitting contribution is important in the *dilute* regime where  $n \lesssim \alpha_s$ . Since, as mentioned previously, the dynamics of the saturation front is driven by the BFKL growth of its dilute tail, these fluctuations play an important role in the 2–gluon density  $\langle nn \rangle$  at high energy.

As manifest in eq. (6), this 2-gluon density enters in the non–linear term leading to saturation of the single gluon density. Thus, gluon number fluctuations in the dilute regime can strongly influence the approach towards saturation. For instance, as argued in (36) for generic reaction–diffusion processes, and independently in the QCD context(37), these fluctuations reduce the (average) speed of the saturation front. Besides making the value of  $Q_s$  a fluctuating quantity, they tend to wash out the geometric scaling property of the individual fronts (38,39). Both effects are quantitatively important, as shown by explicit numerical simulations within various reaction–diffusion models (including those inspired by the QCD dynamics at high energy (40)).

There is presently no general theory that includes BFKL ladders, saturation and fluctuations. (In terms of Feynman graphs, this corresponds to resumming “Pomeron loops” diagrams to all orders (39).) Attempts to construct such a theory (39,41,42) have led to incomplete formalisms that are difficult to exploit in phenomenological applications. Fortunately, the effect of these fluctuations is considerably reduced by the running of the strong coupling (43), which tends to postpone their importance to unrealistically large rapidities. Thus, for practical applications at least up to LHC energies, a sufficient theory for the approach towards saturation is the leading–order mean-field evolution extended with running coupling corrections. This theory has developed significantly as the running–coupling version of the BK equation has been constructed in (44) and successfully applied to studies of the phenomenology at HERA (45).

### 3 Collisions in the CGC framework

The CGC is an effective theory for the wavefunction of a high-energy hadron or nucleus. In this section, we apply it, with particular emphasis on factorization, to deeply inelastic scattering and hadronic collisions. In A+A collisions, the formation of the Glasma and its key features are emphasized.

#### 3.1 The CGC and DIS at small $x$

At small  $x$ , corresponding to large Ioffe times (46), DIS is characterized by the fluctuation of the virtual photon into a quark–antiquark pair which then scatters off the hadronic or nuclear target. The inclusive DIS cross-section can be expressed as (47)

$$\sigma_{\gamma^*T} = \int_0^1 dz \int d^2\mathbf{r}_\perp |\psi(z, \mathbf{r}_\perp)|^2 \sigma_{\text{dipole}}(x, \mathbf{r}_\perp), \quad (10)$$

where  $\psi(z, \mathbf{r}_\perp)$  is the  $q\bar{q}$  component of the wave-function of the virtual photon (known from QED) and  $\sigma_{\text{dipole}}(x, \mathbf{r}_\perp)$  is the QCD “dipole” cross-section for the quark-antiquark pair to scatter off the target. This process is shown in figure 4, where we have assumed that the target moves in the  $-z$  direction. In the leading order (LO) CGC description of DIS, the target is described, as illustrated in figure 5, as static sources with  $k^- > \Lambda_0^-$ . The field modes do not contribute at this order.

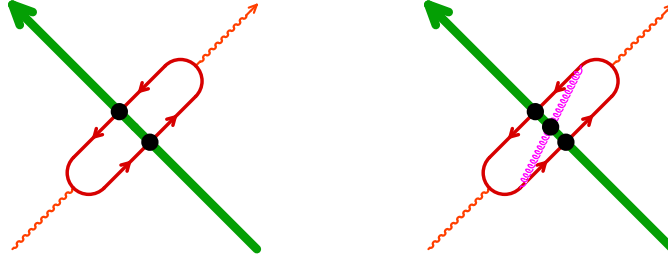


Figure 4: *Left: leading Order (LO) contribution to DIS off the CGC. Right: NLO contribution.*

Employing the optical theorem,  $\sigma_{\text{dipole}}(x, \mathbf{r}_\perp)$  can be expressed in terms of the forward scattering amplitude  $\mathbf{T}(\mathbf{x}_\perp, \mathbf{y}_\perp)$  of the  $q\bar{q}$  pair at LO as

$$\sigma_{\text{dipole}}^{\text{LO}}(x, \mathbf{r}_\perp) = 2 \int d^2\mathbf{b} \int [D\rho] W_{\Lambda_0^-}[\rho] \mathbf{T}_{\text{LO}}(\mathbf{b} + \frac{\mathbf{r}_\perp}{2}, \mathbf{b} - \frac{\mathbf{r}_\perp}{2}), \quad (11)$$

where, for a fixed configuration of the target color sources (48, 49)

$$\mathbf{T}_{\text{LO}}(\mathbf{x}_\perp, \mathbf{y}_\perp) = 1 - \frac{1}{N_c} \text{tr}(U(\mathbf{x}_\perp)U^\dagger(\mathbf{y}_\perp)), \quad (12)$$



with  $U(\mathbf{x}_\perp)$  a Wilson line representing the interaction between a quark and the color fields of the target, defined to be

$$U(\mathbf{x}_\perp) = \text{T exp } ig \int^{1/xP^-} dz^+ \mathcal{A}^-(z^+, \mathbf{x}_\perp). \quad (13)$$

In this formula,  $\mathcal{A}^-$  is the minus component of the gauge field generated (in Lorenz gauge) by the sources of the target; it is obtained by solving classical Yang-Mills equations with these sources. The upper bound  $xP^-$  (where  $P^-$  is the target longitudinal momentum and  $x$  the kinematic variable defined in figure 1) indicates that source modes with  $k^- < xP^-$  do not contribute to this scattering amplitude. Thus if the cutoff  $\Lambda_0^-$  of the CGC EFT is lower than  $xP^-$ ,  $\mathbf{T}_{\text{LO}}$  is independent of  $\Lambda_0^-$ .

However, when  $\Lambda_0^-$  is larger than  $xP^-$ , the dipole cross-section is in fact independent of  $x$  (since the CGC EFT does not have source modes near the upper bound  $xP^-$ ) and depends on the unphysical parameter  $\Lambda_0^-$ . As we shall see now, this is related to the fact that eq. (11) is incomplete and receives large corrections from higher order diagrams. Consider now the NLO contributions (one of them is shown in the right panel in figure 4) with gauge field modes in the slice  $\Lambda_1^- \leq k^- \leq \Lambda_0^-$  (see figure 5). An explicit computation of the contribution of

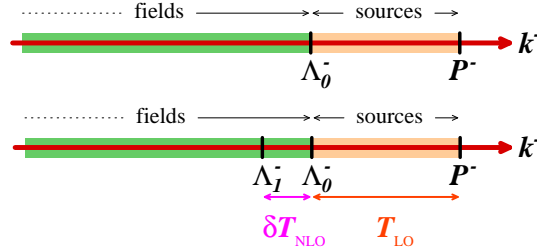


Figure 5: *Top: sources and fields in the CGC effective theory. Bottom: NLO correction from a layer of field modes just below the cutoff.*

field modes in this slice gives

$$\delta \mathbf{T}_{\text{NLO}}(\mathbf{x}_\perp, \mathbf{y}_\perp) = \ln \left( \frac{\Lambda_0^-}{\Lambda_1^-} \right) \mathcal{H} \mathbf{T}_{\text{LO}}(\mathbf{x}_\perp, \mathbf{y}_\perp), \quad (14)$$

where  $\mathcal{H}$  is the JIMWLK Hamiltonian. All dependence on the cutoff scales is in the logarithmic prefactor alone. This Hamiltonian has two derivatives with respect to the classical field  $\mathcal{A} \sim \mathcal{O}(1/g)$ ;  $\mathcal{H} \mathbf{T}_{\text{LO}}$  is of order  $\alpha_s \mathbf{T}_{\text{LO}}$  and therefore clearly an NLO contribution. However, if the new scale  $\Lambda_1^-$  is such that

$\alpha_s \ln(\Lambda_0^-/\Lambda_1^-) \sim 1$ , this NLO term becomes comparable in magnitude to the LO contribution. Averaging the sum of the LO and NLO contributions over the distribution of sources at the scale  $\Lambda_0^-$ , one obtains

$$\int [D\rho] W_{\Lambda_0^-}[\rho] (\mathbf{T}_{\text{LO}} + \delta\mathbf{T}_{\text{NLO}}) = \int [D\rho] W_{\Lambda_1^-}[\rho] \mathbf{T}_{\text{LO}}, \quad (15)$$

where  $W_{\Lambda_1^-} \equiv (1 + \ln(\Lambda_0^-/\Lambda_1^-) \mathcal{H}) W_{\Lambda_0^-}$ . We have shown here that the NLO correction from quantum modes in the slice  $\Lambda_1^- \leq k^- \leq \Lambda_0^-$  can be absorbed in the LO term, provided we now use a CGC effective theory at  $\Lambda_1^-$  with the modified distribution of sources shown in eq. (15). In differential form, the evolution equation of the source distribution,

$$\frac{\partial}{\partial \ln(\Lambda^-)} W_{\Lambda^-} = -\mathcal{H} W_{\Lambda^-}, \quad (16)$$

is the JIMWLK equation.

Repeating this elementary step, one progressively resums quantum fluctuations down to the scale  $k^- \sim xP^-$ . Thanks to eq. (15), the result of this resummation for the dipole cross-section is formally identical to eq. (11), except that the source distribution is  $W_{xP^-}$  instead of  $W_{\Lambda_0^-}$ . Note that if one further lowers the cutoff below  $xP^-$ , the dipole cross-section remains unchanged.

### 3.2 The CGC in p+A collisions

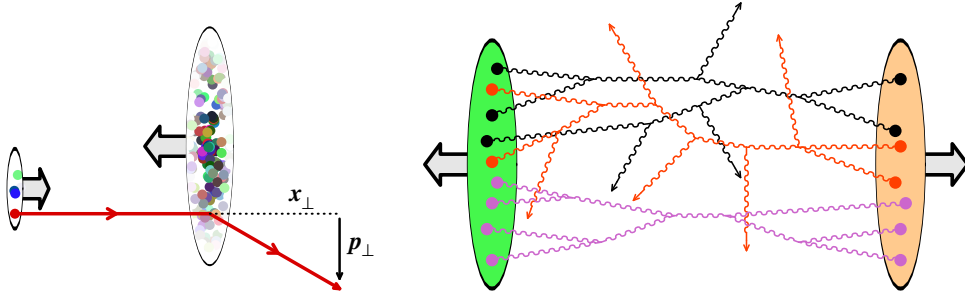


Figure 6: *Left: sketch of a proton-nucleus collision. Right: example of leading order contribution in a nucleus-nucleus collision.*

Collisions between a dilute hadron projectile and a dense hadron target can be studied semi-analytically in the CGC framework. The archetype of such collisions is a proton-nucleus collision. However, the dilute-dense treatment also applies to proton-proton collisions for measurements at forward rapidities where the wavefunction of one of the projectiles is probed at large  $x$  and that of the other at

small  $x$ . These asymmetrical collisions can be treated using conventional parton distributions for the proton and the CGC for the nucleus.

The simplest quantity to compute in this context is the single particle inclusive spectrum. In the CGC framework, this process is due to the scattering of a parton from the proton off the color field of the target nucleus, as illustrated in figure 6 (left). When the parton is a quark, the amplitude for the scattering is proportional to the Fourier transform of a Wilson line,

$$\mathcal{M}_{\text{LO}} \propto \int d^2\mathbf{x}_\perp e^{i\mathbf{p}_\perp \cdot \mathbf{x}_\perp} U(\mathbf{x}_\perp). \quad (17)$$

Squaring this amplitude, summing over the color of the quark in the final state and averaging over the color of the incoming quark, we get

$$|\mathcal{M}|_{\text{LO}}^2 \propto \int d^2\mathbf{b} d^2\mathbf{r}_\perp e^{i\mathbf{p}_\perp \cdot \mathbf{r}_\perp} \mathbf{T}_{\text{LO}} \left( \mathbf{b} + \frac{\mathbf{r}_\perp}{2}, \mathbf{b} - \frac{\mathbf{r}_\perp}{2} \right), \quad (18)$$

where  $\mathbf{T}_{\text{LO}}$  is the dipole scattering amplitude (see eq. (12)) that already appeared in our discussion of DIS. Because the same quantity appears here, the treatment of the NLO corrections we described in the DIS case is similarly applicable; one integrates out softer modes by lowering the cutoff of the CGC EFT letting  $W_{\Lambda^-}[\rho]$  evolve according to the JIMWLK equation. The scale to which one evolves the cutoff is  $\Lambda^- = xP^-$  with  $x = (p_\perp/\sqrt{s}) \exp(-y)$  where  $p_\perp$  is the transverse momentum of the scattered parton and  $y$  its rapidity. Therefore, in the CGC framework, the cross-section for this process is simply the Fourier transform of the dipole cross-section  $\sigma_{\text{dipole}}(x, \mathbf{r}_\perp)$ . In p+A collisions, final states containing a photon or a lepton pair can be similarly expressed in terms of the same Fourier transform (50).

An additional contribution to the single inclusive particle spectrum in a p+A collision is due to an incoming gluon instead of a quark. The treatment is nearly identical to the incoming quark case, except that in eq. (17) one must replace the Wilson line in the fundamental representation by a Wilson line in the adjoint representation.

Similar calculations can be performed for processes with more complicated final states, such as the production of a quark-antiquark pair. Although this observable has a more complicated expression (containing terms that are the product of four Wilson lines) its NLO corrections still comply with eq. (14), which ensures their factorization into the distribution of sources  $W_{\Lambda^-}[\rho]$ . The crucial ingredient for factorization to work is to consider an observable that is sufficiently inclusive to allow the corresponding final state to be accompanied by an arbitrary number

of gluons. Any restriction on associated gluon radiation will not permit NLO corrections to factorize simply in the distribution of sources.

A much more limited but widely used form of factorization is  $k_{\perp}$  factorization (51) in terms of  $k_{\perp}$  dependent unintegrated quark and gluon distributions of the projectile and target. Within the CGC framework, these results can be reproduced for gluon (52,53) and heavy quark (54) distributions at large transverse momenta  $k_{\perp} \geq Q_s$ ; however, at smaller transverse momenta,  $k_{\perp}$  factorization is broken even at leading order (55–57).

### 3.3 Shattering CGCs in A+A collisions

Collisions between two nuclei (“dense-dense” scattering) are complicated to handle on the surface. However, in the CGC framework, because the wave functions of the two nuclei are saturated, the collision can be treated as the collision of classical fields. This insight significantly simplifies the treatment of A+A scattering. The classical fields are coupled to fast partons of each nucleus respectively described by the external current  $J^{\mu} = \delta^{\mu+} \rho_1 + \delta^{\mu-} \rho_2$ . The source densities of fast partons  $\rho_{1,2}$  are both parametrically of order  $1/g$ , which implies that graphs involving multiple sources from both projectiles must be resummed. (See the right panel of figure 6 for an illustration.)

At leading order, inclusive observables<sup>6</sup> depends on the retarded classical color field  $\mathcal{A}^{\mu}$ , which solves the Yang-Mills equations  $[\mathcal{D}_{\mu}, \mathcal{F}^{\mu\nu}] = J^{\nu}$  with the boundary condition  $\lim_{x^0 \rightarrow -\infty} \mathcal{A}^{\mu} = 0$ . Among the observables to which this result applies is the expectation value of the energy-momentum tensor at early times after the collision. At leading order,

$$T_{\text{LO}}^{\mu\nu} = \frac{1}{4} g^{\mu\nu} \mathcal{F}^{\lambda\sigma} \mathcal{F}_{\lambda\sigma} - \mathcal{F}^{\mu\lambda} \mathcal{F}^{\nu}_{\lambda}, \quad (19)$$

where  $\mathcal{F}^{\mu\nu}$  is the field strength of the classical field  $\mathcal{A}^{\mu}$ .

Although A+A collisions are more complicated than e+A or p+A collisions, one can still factorize the leading higher order corrections into the evolved distributions  $W_{\Lambda-}[\rho_1]$  and  $W_{\Lambda+}[\rho_2]$ . At the heart of this factorization is a generalization of eq. (14) to the case where the two projectiles are described in the CGC framework (58). When one integrates out the field modes in the slices

---

<sup>6</sup>Exclusive observables may also be expressed in terms of solutions of the same Yang-Mills equations, but with more complicated boundary conditions than for inclusive observables.

$\Lambda_1^\pm \leq k^\pm \leq \Lambda_0^\pm$ , the leading correction to the energy momentum tensor is

$$\delta T_{\text{NLO}}^{\mu\nu} = \left[ \ln \left( \frac{\Lambda_0^-}{\Lambda_1^-} \right) \mathcal{H}_1 + \ln \left( \frac{\Lambda_0^+}{\Lambda_1^+} \right) \mathcal{H}_2 \right] T_{\text{LO}}^{\mu\nu}, \quad (20)$$

where  $\mathcal{H}_{1,2}$  are the JIMWLK Hamiltonians of the two nuclei respectively. What is crucial here is the absence of mixing between the coefficients  $\mathcal{H}_{1,2}$  of the logarithms of the two projectiles; they depend only on  $\rho_{1,2}$  respectively and not on the sources of the other projectile. Although the proof of this expression is somewhat involved, the absence of mixing is deeply rooted in causality. The central point is that because the duration of the collision (which scales as the inverse of the energy) is so brief, soft radiation must occur before the two nuclei are in causal contact. Thus logarithms associated with this radiation must have coefficients that do not mix the sources of the two projectiles.

Following the same procedure for eq. (20), as for the e+A and p+A cases, one obtains for the energy-momentum tensor in an A+A collision the expression

$$\langle T^{\mu\nu} \rangle_{\text{LLog}} = \int [D\rho_1 D\rho_2] W_1[\rho_1] W_2[\rho_2] T_{\text{LO}}^{\mu\nu}. \quad (21)$$

This result can be generalized to multi-point correlations of the energy-momentum tensor,

$$\begin{aligned} \langle T^{\mu_1\nu_1}(x_1) \cdots T^{\mu_n\nu_n}(x_n) \rangle_{\text{LLog}} &= \int [D\rho_1 D\rho_2] W_1[\rho_1] W_2[\rho_2] \\ &\quad \times T_{\text{LO}}^{\mu_1\nu_1}(x_1) \cdots T_{\text{LO}}^{\mu_n\nu_n}(x_n). \end{aligned} \quad (22)$$

In this expression, all the correlations between the energy-momentum tensor at different points are from the distributions  $W_{1,2}[\rho_{1,2}]$ . Thus, the leading correlations are already built into the wavefunctions of the projectiles prior to the collision.

The expressions in eqs. (21) and (22) are valid for proper times  $\tau \sim 1/Q_s$  after the heavy ion collision. The energy-momentum tensor, for each configuration of sources  $\rho_{1,2}$  is determined by solving classical Yang–Mills equations to compute the gauge fields  $\mathcal{A}_\mu^{\text{cl}}[\rho_1, \rho_2]$  in the forward light cone with initial conditions determined by the classical CGC fields of each of the nuclei at  $\tau = 0$  (55, 59–62). The corresponding non-equilibrium matter, with high occupation numbers  $\sim 1/\alpha_s$  is called the Glasma (63). The Glasma fields at early times are longitudinal chromo-electric and chromo-magnetic fields that are screened at distances  $1/Q_s$  in the transverse plane of the collision. As a consequence, the matter produced can be visualized (see figure 7) as comprising  $R_A^2 Q_s^2$  color flux tubes of size  $1/Q_s$ , each producing  $1/\alpha_s$  particles per unit rapidity. The flux tube picture is sup-

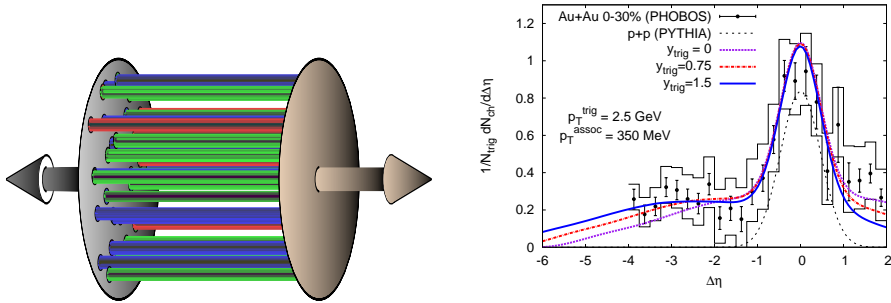


Figure 7: *Left: Gauge field configurations in the form of “flux tubes” of longitudinal chromo-electric and chromo-magnetic fields screened on transverse scales  $1/Q_s$ . Right: Model comparison (64) to long range rapidity correlations measured by the PHOBOS collaboration (65).*

ported by non-perturbative numerical solutions of the classical Yang-Mills equations (66). The “Glasma flux tubes” generate  $n$ -particle long range rapidity correlations (58, 64, 67, 68). These distributions are negative binomial distributions (69). They also carry topological charge (70); the resulting dynamical topological “sphaleron” transitions may result in observable metastable CP-violating domains (71).

The evolution of the Glasma into a thermalized Quark Gluon Plasma (QGP) is not understood. An important ingredient is the role of instabilities (72). At early times, these arise at NLO from terms that break the boost invariance of the LO term (10, 58). The modification to the evolution of the Glasma is obtained by solving 3+1-D Yang-Mills equations (73) for the (now) rapidity dependent gauge fields convolved with a distribution giving the spectrum of fluctuations (74). While these effects may isotropize the system, early thermalization may also require collisions whose role still needs to be clarified (75).

#### 4 Phenomenological applications of the CGC

In this section, we will discuss the applications of the theoretical formalism outlined in the previous section to analyze and *predict* a wide range of phenomena ranging from DIS in e+p and e+A collisions to the scattering of hadronic projectiles ranging from p+p to p+A to A+A collisions. A unifying ingredient in many of the applications is the dipole cross-section defined in eq. (11), albeit, as apparent in the treatment of A+A collisions, the fundamental ingredient is really the density matrix  $W_Y[\rho]$ . Because the JIMWLK equation (eq. (16)) for

this quantity is time consuming to solve<sup>7</sup>, many of the applications are in the context of models of the dipole cross-section which incorporate key features of saturation. These models provide an economical description of a wide range of data with only a few parameters. A good compromise between the full JIMWLK dynamics and models of the dipole cross-section is the BK equation, which is a large  $N_c$  realization of JIMWLK dynamics. With the recent availability of the NLO BK equation, global analyzes of data are in order. Much of our discussion below is in the context of dipole models; improvements *a la* BK are highlighted wherever available.

#### 4.1 DIS in e+p and e+A collisions

A remarkable observation (25) is that HERA data (25,26) on the inclusive virtual photon-proton cross section for  $x \leq 0.01$  scale as a function of the ratio  $Q^2/Q_s^2(x)$ ; see the left part of figure 8. This scaling is violated for larger values of  $x$ . Here  $Q_s^2 = Q_0^2(x_0/x)^\lambda$  is the saturation scale with  $Q_0^2 = 1 \text{ GeV}^2$ ,  $x_0 = 3 \cdot 10^{-4}$  and  $\lambda \approx 0.3$ . This scaling is referred to as “geometrical scaling”, because the survival probability of the color dipole that the virtual photon fluctuates into is close to unity or zero respectively depending on whether the ratio of the saturation radius ( $\sim 1/Q_s$ ) to the size of the dipole (of size  $\sim 1/Q$ ) is large or small. Recall that the saturation radius denotes the typical size of regions with strong color fields. Geometric scaling has also been observed in inclusive diffraction, exclusive vector meson production and deeply virtual Compton scattering data at HERA (78). In detail, the data also show *violations* of geometric scaling, which can be interpreted as consequences of BFKL diffusion (79), non-zero quark masses (80) and possibly DGLAP evolution as well (81). Note that the best scaling is obtained with a saturation scale that behaves like  $Q_s^2(x) \propto x^{-0.3}$ , a slower  $x$ -dependence than predicted by the LO BK equation. This discrepancy is resolved by a resummed NLO computation of the saturation exponent (24) which indeed gives 0.3.

While geometrical scaling is very suggestive of the presence of semi-hard dynamical scales in the proton, it is not conclusive in and of itself (82); more detailed comparisons to the data are essential. Despite their simplicity, saturation models (45,79–81,83–86) provide remarkably good descriptions of HERA data at small  $x \leq 0.01$ . The free parameters are fixed from fits to the total cross-section data

---

<sup>7</sup>Other unknowns include higher order corrections, initial conditions at low energy and impact-parameter dependence of distributions.

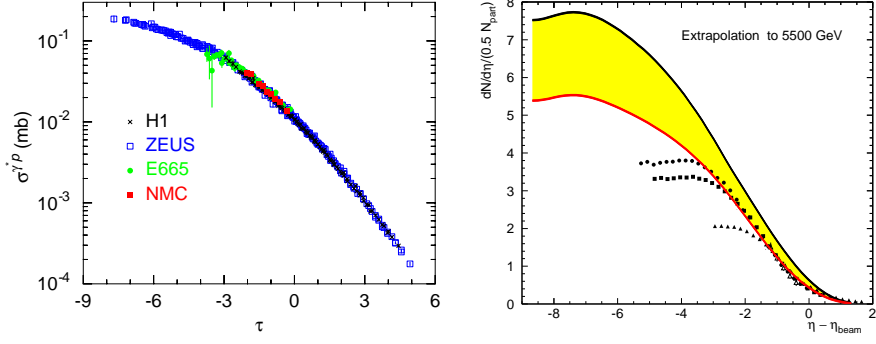


Figure 8: *Geometrical scaling and limiting fragmentation.* Left:  $\sigma_{\gamma^*p}$  data at HERA for  $x \leq 0.01$  and all  $Q^2$  up to  $450 \text{ GeV}^2$ ;  $\tau$  is the scaling variable,  $\tau \equiv Q^2/Q_s^2(x)$  (25, 26). Right: particle multiplicities for several collision energies at RHIC (76), compared to the computation of (77).

alone; once these are fixed, the models *predict* a large variety of results, including the longitudinal ( $F_L$ ), diffractive ( $F_2^D$ ), and charm ( $F_2^c$ ) structure functions, the virtual photon production of vector mesons ( $\rho$ ,  $J/\psi$ ), and the deeply virtual Compton scattering (DVCS). The most recent analysis of inclusive data (45) of DIS in e+p collisions is quite sophisticated; the energy dependence is given by the running-coupling BK equation, and the free parameters refer solely to the initial conditions and to the proton transverse area.

The phenomenon of *hard diffraction* in DIS is particularly sensitive to saturation. The simplest diffractive processes are events in which the proton remains intact and a large gap in rapidity with no particles extends between the rapidity of the proton and that of the fragmentation products of the virtual photon. For small invariant masses, this process corresponds to elastic scattering of the  $q\bar{q}$  dipole off the target. Its cross-section is evaluated as<sup>8</sup>

$$\left. \frac{d\sigma_{\text{diff}}}{dt} \right|_{t=0} = \frac{1}{16\pi} \int_0^1 dz \int d^2\mathbf{r}_\perp |\psi(z, \mathbf{r}_\perp)|^2 \sigma_{\text{dipole}}^2(x, \mathbf{r}_\perp). \quad (23)$$

The dipole cross-section in this expression, for small dipoles  $r^2 \ll 1/Q_s^2$ , is a color singlet combination of two gluons that can be interpreted as Pomeron exchange (87); for larger dipoles  $r^2 \geq 1/Q_s^2$ , the color singlet exchange does not have this simple interpretation. The  $t$  distribution has the form  $d\sigma_{\text{diff}}/dt =$

<sup>8</sup>Forward diffraction (corresponding to  $t = 0$ , where  $t = (P - P')^2$  is the momentum transfer squared between the incoming and outgoing proton) can be compared directly to inclusive DIS within a dipole model since it depends only on the dipole cross-section.



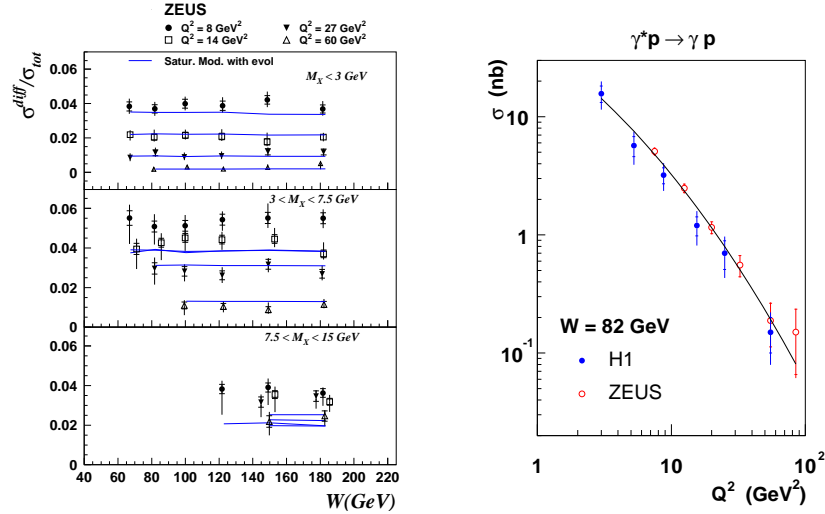


Figure 9: *Left*: ZEUS data for the ratio  $\sigma_{\text{diff}}/\sigma_{\text{tot}}$  together with the corresponding prediction of the saturation model in (84). *Right*: DVCS measurement at HERA, and comparison with (81).

$\exp(-B_D|t|)d\sigma_{\text{diff}}/dt|_{t=0}$ , where  $B_D$  is the transverse area of the interaction region in the proton and is closely related to the transverse gluon radius in the proton estimated to be  $0.61 \pm 0.04$  fm (88). From this form of the diffractive cross-section and eq. (23), the total diffractive cross-section is

$$\sigma_D \sim \frac{B_D}{Q^2} \int_{Q^{-2}}^{Q_s^{-2}} \frac{dr^2}{r^4} \left( r^2 Q_s^2(x) \right)^2 \sim B_D \frac{Q_s^2(x)}{Q^2}. \quad (24)$$

We used here the color transparency approximation  $\sigma_{\text{dipole}} \propto r^2 Q_s^2(x)$  for the dipole cross-section. Unlike the inclusive cross-section in eq. (10) which is dominated by small dipole sizes  $\sim 1/Q$ , the integrand of the diffractive cross-section is dominated by larger size dipoles of size  $\sim 1/Q_s$ . Comparing eq. (24) with eq. (10), we deduce that in the saturation framework the ratio  $\sigma_{\text{diff}}/\sigma_{\text{tot}}$  is approximately constant as a function of energy. As shown in figure 9 (left), the HERA data support this qualitative observation and are in quantitative agreement with the detailed saturation model of (84). We note further that excellent fits with  $\chi^2 \sim 1$  are obtained in this saturation framework for exclusive vector meson production and deeply virtual Compton scattering (81) in addition to inclusive diffraction (89) (see figure 9, right). These exclusive processes provide detailed information about the impact parameter dependence of the dipole cross-section (90) and may even provide unique information about the partonic nature

of short range nuclear forces (88).

In contrast, if unitarization were due to soft physics (the prevailing viewpoint before the advent of saturation (91)), the natural cutoff for the integral would be  $1/\Lambda_{\text{QCD}}$ . Diffraction would be non-perturbative even for hard  $Q$  and the energy dependence of the diffractive cross-section would be the square of the inclusive cross-section, in disagreement with data.

Fits based on geometrical scaling of the e+A fixed target data with the functional form  $Q_s^2 \propto A^\delta$  (with  $\delta$  naively 1/3) give values of  $\delta$  with range from 1/4 to 4/9 (92). However, the dipole formalism which describes e+p data so successfully can be straightforwardly generalized to nuclei to construct the corresponding nuclear dipole cross-section (85). When compared to results for the  $x, Q^2$  dependence of inclusive e+A data, one finds effectively that  $Q_{s,A}^2(x) = Q_{s,p}^2(x)A^{1/3}$  (93). Nuclear diffractive distributions can be computed in saturation models (89,94); predictions have been made as well for semi-inclusive hadron production (95), exclusive vector meson production (96) and nuclear DVCS (97) in this framework.

In saturation models of nuclei, the small  $x$  distributions in a nucleon are convolved with nuclear geometry to give the nuclear distributions. This process however does not commute with the RG evolution in  $x$  of nuclear distributions determined at some initial scale. First computations of e+A inclusive distributions in the NLO BK framework have been performed and good agreement obtained for existing fixed target data (64).

## 4.2 Particle multiplicities in d+A and A+A collisions

The CGC EFT is most reliable when at least one of the projectiles is dense in the sense discussed in the previous section. At RHIC, the world's first deuteron+heavy nucleus (d+A) and A+A collider, many features of the CGC are being tested. These include bulk features such as the rapidity and centrality dependence of particle multiplicities in d+A and A+A collisions, limiting fragmentation, particle spectra and correlations, and even possibly more exotic features such as long range rapidity correlations (“the ridge”) in A+A collisions and local CP violation arising from topological fluctuations in A+A collisions. In this sub-section, we will focus on particle multiplicities and discuss the other features in subsequent sub-sections.

“Limiting fragmentation” is the well known property of the strong interactions that the rapidity distribution in the fragmentation region becomes independent

of the collision energy. When one increases the beam energy (see figure 8, right),  $dN/d\eta'$  is the same at large  $\eta'$  for all energies, where  $\eta' \equiv \eta - \eta_{\text{beam}}$ . In the fragmentation region, large  $x_1$  modes are probed in one hadron or nucleus and small  $x_2$  modes in the other. At small  $x_2$ , if gluonic matter is saturated, parton distributions have a very weak dependence on  $x_2$ , or equivalently on  $\eta + \eta_{\text{beam}}$ ; cross-sections will only depend on  $x_1$  or  $\eta - \eta_{\text{beam}}$ . Deviations from limiting fragmentation at high energies are especially interesting because of a significant window in phase space where the RG evolution in  $x_2$  to (or away) from the universal “black disk” of saturated gluon matter can be explored (77, 98). These constraints lead to specific predictions for the rapidity dependence of the multiplicity at the LHC in the BK RG framework (77, 99).

The CGC can only predict the distribution of initial gluons, at a proper time  $\tau \sim Q_s^{-1}$ . In p/d+A collisions this is not a significant limitation because only a few gluons are produced in the final state. The situation is vastly different in A+A collisions where the particle multiplicity is significantly larger and the system evolves from the non-equilibrium Glasma to a QGP, the latter evolving subsequently as a fluid with low viscosity. For p+A collisions, the problem is solvable analytically (52, 53, 100). For A+A collisions, two kinds of calculations have been performed:

(a) Exact numerical solutions of the Yang-Mills equations (55, 59, 61). Quantum evolution effects are not included systematically and the ensemble of color charges is assumed to be Gaussian (MV model), which is reasonable at RHIC energies of  $x \sim 10^{-2}$  at RHIC. The inclusion of quantum effects from the wavefunctions (58, 69) is under control, but is still an unsolved problem for those present in the final state evolution (73, 74).

(b) Approximate analytical calculations of the initial gluon spectrum (101). These calculations assume  $k_{\perp}$ -factorization although it is violated for momenta  $p_{\perp} \leq Q_s$ . In this model, saturation effects are introduced via the unintegrated gluon distribution of the nuclei with the rapidity dependence of the gluon spectrum governed by that of the saturation scale  $Q_s^2(x) \sim x^{-0.3}$ . In the CGC framework,  $dN/d\eta = Q_s^2 R_A^2 / \alpha_s(Q_s)$ ; a unique feature is that the coupling runs as a function of  $Q_s$  (102), an observation which is in agreement with the centrality dependence of RHIC data (103). Similar analyzes of multiplicity distributions were extended to the case of d+A collisions (104), with results in fair agreement with RHIC data.

### 4.3 Inclusive spectra in d+A and A+A collisions

4.3.1  $p_{\perp}$  DEPENDENCE One does not expect significant final state interactions with on-shell partons in  $p + A$  collisions. Moreover, the inclusive gluon spectrum depends only on the Wilson line correlator  $\langle U(0)U^{\dagger}(\mathbf{x}_{\perp}) \rangle$  (53,100,105), that can be determined from the dipole cross-section used in DIS (106). The hadron spectrum in d+A collisions has been evaluated in this approach in (107), with results in good agreement with RHIC data. Very recently, good agreement of single inclusive distributions in d+A collisions were obtained in the NLO RG approach (108) consistent with its application in e+A collisions (64).

In A+A collisions, the strong final state interactions likely alter the momentum distribution to be more isotropic at low momenta; the hard tail is modified by parton energy loss. While these effects may in part be included in the Glasma, the additional contributions at later stages are important.

4.3.2 NUCLEAR MODIFICATION RATIOS To quantify nuclear effects,  $p_{\perp}$  spectra in A+A and d+A can be compared to those in p+p collisions by the ratios

$$R_{AA} \equiv \frac{\frac{dN}{dyd^2\mathbf{p}_{\perp}} \Big|_{AA}}{N_{\text{coll}} \frac{dN}{dyd^2\mathbf{p}_{\perp}} \Big|_{pp}}, \quad R_{dA} \equiv \frac{\frac{dN}{dyd^2\mathbf{p}_{\perp}} \Big|_{dA}}{N_{\text{coll}} \frac{dN}{dyd^2\mathbf{p}_{\perp}} \Big|_{pp}}, \quad (25)$$

where  $N_{\text{coll}} \sim A^{4/3}$  (resp.  $A$ ) is the number of binary collisions in A+A (resp. d+A) collisions. At high  $p_{\perp}$ , one expects the ratios to scale with  $N_{\text{coll}}$ . In A+A collisions at RHIC, because no suppression is seen in d+A collisions at central rapidities, the large observed suppression in  $R_{AA}$  is rightly interpreted as a final state effect, with a strong candidate being energy loss induced by the dense medium (109).

However, at small  $x$ , RG evolution *a la* BK predicts (110) that this ratio should be suppressed by saturation effects in the wavefunction of the nucleus. This can be studied in the clean environment of d+A collisions where small  $x$  is probed measuring the ratio at a positive rapidity in the direction of the deuterium nucleus. The ratio  $R_{dA}$  was measured by the BRAHMS (111) collaboration up to rapidities of  $\eta = 3.2$  and by the STAR collaboration (112) at  $\eta = 4$ . At these large  $\eta$ , the value of  $R_{dA}$  is significantly below unity, consistent with predicted trend. In addition, as anticipated, the suppression is greater for more central collisions. The onset of this forward suppression was also studied semi-analytically in (100,113), and more quantitative calculations have been performed in (107,114,115), using models of the dipole cross-section that have a realistic  $x$ -dependence and most recently in the NLO BK framework (108).

#### 4.4 Two hadron correlations in d+A and A+A collisions

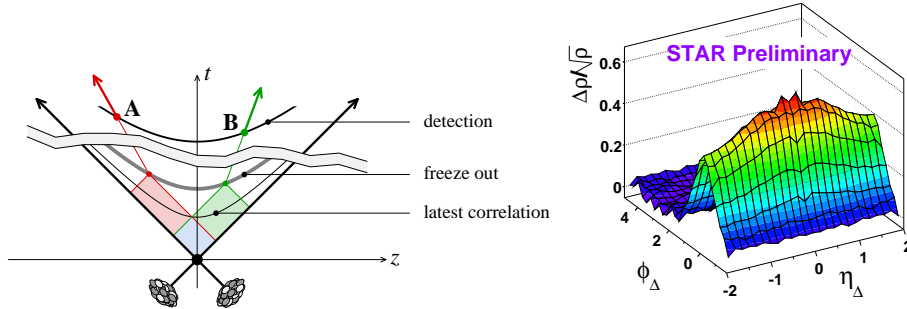


Figure 10: Left: causal relations between two particles separated in rapidity. Right: 2-hadron correlation measured by STAR as a function of  $\Delta\eta$  and  $\Delta\phi$ .

Two hadron correlations<sup>9</sup> are more sensitive in distinguishing between model predictions than the single inclusive results for which alternative explanations of the data are feasible. Very recently, striking preliminary results on these correlations in d+Au collisions have been presented by the STAR and PHENIX collaborations. In the STAR measurements, back-to-back correlations of pairs have been studied where i) one particle in the pair is forward in rapidity and the other at central rapidity and ii) both particles in the pair are at forward rapidities. The “forward-central” (FC) pairs probe  $x \sim 10^{-2}$  in the gold nucleus while the “forward-forward” (FF) pairs probe  $x \sim 10^{-3}$  in the gold nucleus. A clear broadening of the backward hadron peak is seen in the transition from FC to FF, as well as with increasing centrality in the FF events—in the latter case, the distribution is so broad that no peak is visible! This particular effect was predicted in the CGC (117) and is in quantitative agreement the STAR results (118). These results are also consistent with measurements by the PHENIX collaboration on pair distributions in d+Au collisions. Related discussions can be found in (119).

While two particle correlations in A+A collisions are typically much altered by final state interactions, there is an important exception for particles widely separated in rapidity. Causality implies that these correlations are created at very early times, as illustrated in the left panel of figure 10. A simple estimate for ultra-relativistic particles whose space-time and momentum rapidities are strongly correlated gives

$$\tau_{\max} = \tau_{\text{freezeout}} e^{-\frac{|\Delta\eta|}{2}}, \quad (26)$$

<sup>9</sup>Hadron-photon correlations have also been studied in (116).

for the latest time at which these particles could have been correlated. For a freeze-out time  $\tau_{\text{freezeout}} \approx 10 \text{ fm}/c$ , and rapidity separations  $\Delta\eta \geq 4$ , one sees that these correlations must have been generated before  $1 \text{ fm}/c$ . Thus long range rapidity correlations are a “chronometer” of the evolution of the very strong Glasma color fields produced early in the heavy ion collision.

Striking long range rapidity correlations were seen in A+A collisions in events with prominent jet like structures, where the spectrum of associated particles is observed to be collimated in the azimuthal separation  $\Delta\varphi$  relative to the jet and shows a nearly constant amplitude in the strength of the pseudo-rapidity correlation  $\Delta\eta$  up to  $\Delta\eta \sim 1.5$  (120). These events were coined “ridge” events following from the visual appearance of these structures as an extended mountain ridge in the  $\Delta\eta$ - $\Delta\varphi$  plane associated with a narrow jet peak. This collimated correlation persists up to  $\Delta\eta \sim 4$  (65,121). An important feature of ridge correlations is that the above described structure is seen in two particle correlations without a jet trigger (see figure 10) and persists without significant modification for the triggered events (122,123). These events include all hadrons with momenta  $p_{\perp} \geq 150 \text{ MeV}$ . In such events, a sharp rise in the amplitude of the ridge is seen (122,124) in going from peripheral to central collisions.

The ridge structures seen in two particle and three particle (125) A+A correlations can be explained as resulting from the transverse radial flow of the Glasma flux tubes we discussed previously in section 3.3. The flux tubes are responsible for the long range rapidity correlation in the ridge; the angular collimation occurs because particles produced isotropically in a given flux tube are collimated by the radial outward “Hubble” hydrodynamic flow of the flux tubes. Ideas on the angular collimation of particle distributions by flow were discussed in refs. (126). When combined with the long range rapidity correlations provided by the Glasma flux tubes, they provide a semi-quantitative description of the ridge measurements (64,67,68,127). More detailed studies are feasible with realistic hydrodynamic simulations (128). We note that the PHENIX collaboration which also observed ridge-like structures (129) have presented preliminary data showing that ridge-like structures disappear as the  $p_{\perp}$  of the trigger particle is increased (130); this result is in qualitative agreement with expectations in the Glasma flux tube picture. For a recent critical evaluation of this and alternative models, we refer the reader to (131).

## 5 Outlook: LHC and future DIS colliders

At the LHC, very low values of  $x$  will be probed in p+p, A+A (including the photo-production induced dynamics of peripheral A+A collisions) and possibly p+A collisions through a wide range of final states and diverse kinematic ranges. In nuclei,  $Q_s^2$  will be large; estimates range from  $\sim 2.6$ -4 GeV<sup>2</sup> in central collisions to  $\sim 10$  GeV<sup>2</sup> for  $y = \pm 3$  units. The picture of strongly correlated albeit weakly coupled dynamics of glue in the CGC EFT outlined here will be tested as never before. Detailed tests of BFKL dynamics and possibly even the CGC are feasible in p+p collisions in studies respectively of Mueller-Navelet (132) and forward jets. Diffractive final states, while always challenging to interpret, offer opportunities to understand deeply how saturated gluons generate rapidity gaps. A strong test of CGC dynamics will already be available in “Day 1” physics of bulk dynamics in A+A collisions. More subtle tests of the RG flow of multi-parton correlators are available in a variety of final states ranging from quarkonia to electromagnetic probes to long range rapidity correlations. In p+A collisions at the LHC, many of the patterns seen in forward single inclusive and di-hadron correlation spectra will be present already at central rapidities and will be much more dramatic at forward rapidities. Finally, the role of Glasma dynamics relative to that of the Quark-Gluon Plasma in A+A collisions at the LHC is still unclear. If RHIC has reached the perfect hydrodynamic limit of maximal flow, what happens at the LHC?

Studies of the dynamics of gluon saturation and the CGC that are complementary to the LHC can be performed at a future Electron-Ion Collider (EIC)<sup>10</sup>. Firstly, with a wide lever arm in  $Q^2$ , the dynamics of saturation can be studied with precision in the regime where  $Q^2 \sim Q_s^2 \gg \Lambda_{\text{QCD}}^2$ ; this is difficult to achieve at a hadron collider. Secondly, clarifying what aspects of the dynamics probed are universal and novel calls for an electron probe. The factorization theorems we have developed here suggest that the density matrices  $W$  are universal—how can we confirm this and cleanly extract their rich dynamics? These issues are not merely academic and are strongly reflected in the structure of final states. For example, rapidity gaps are a large fraction of the cross-section at HERA but are a much smaller contribution in hadronic collisions at Fermilab, demonstrating a breakdown of factorization (133). The physics case for an EIC/LHeC has been

---

<sup>10</sup>Current proposals include the EIC in the eRHIC version at BNL and the eLIC version at Jlab, the LHeC proposal at CERN and an electron-ion collider at FAIR in GSI.

outlined in (134) and in a number of white papers and reports.

In summary, the prospects for unambiguous discovery and exploration of a novel many body QCD regime of gluon saturation are very bright in the next decade. The theoretical status of studies of this regime within the framework of the CGC EFT are increasingly robust albeit many questions remain. It is hoped that experiments, as usual, will provide definitive answers.

## Acknowledgements

F.G. and E.I. are supported in part by Agence Nationale de la Recherche via the program ANR-06-BLAN-0285-01. J.J.-M. is supported by the DOE Office of Nuclear Physics through Grant No. DE-FG02-09ER41620 and by the City University of New York through the PSC-CUNY Research Award Program, grant 62625-40. R.V.'s research is supported by the US Department of Energy under DOE Contract No. DE-AC02-98CH10886.

## LITERATURE CITED

1. F. Wilczek, Mod. Phys. Lett. **A 21**, 701 (2006).
2. G. Altarelli, G. Parisi, Nucl. Phys. **B 126**, 298 (1977); V.N. Gribov, L.N. Lipatov, Sov. J. Nucl. Phys. **15**, 438 (1972); *ibid.* 675 (1972); Yu. Dokshitzer, Sov. Phys. JETP **46**, 641 (1977).
3. F.D. Aaron, et al, [H1 Collaboration] Eur. Phys. J. **C 64**, 561 (2009).
4. A. Donnachie, P.V. Landshoff, Phys. Lett. **B 437**, 408 (1998).
5. L.N. Lipatov, Sov. J. Nucl. Phys. **23**, 338 (1976); E.A. Kuraev, L.N. Lipatov, V.S. Fadin, Sov. Phys. JETP **45**, 199 (1977); I. Balitsky, L.N. Lipatov, Sov. J. Nucl. Phys. **28**, 822 (1978);
6. L.V. Gribov, E.M. Levin, M.G. Ryskin, Phys. Rept. **100**, 1 (1983); A.H. Mueller, J.-W. Qiu, Nucl. Phys. **B 268**, 427 (1986).
7. A.M. Stasto, Int. J. Mod. Phys. **A 19**, 317 (2004); H.J. Drescher, A. Du-



- mitru, M. Strikman, Phys. Rev. Lett. **94**, 231801 (2005); A. Cooper-Sarkar, S. Sarkar, JHEP **0801**, 075 (2008); E.M. Henley, J. Jalilian-Marian, Phys. Rev. **D 73**, 094004 (2006).
8. E. Iancu, A. Leonidov, L.D. McLerran, hep-ph/0202270; E. Iancu, R. Venugopalan, hep-ph/0303204.
  9. J. Jalilian-Marian, Y. Kovchegov, Prog. Part. Nucl. Phys. **56**, 104 (2006); H. Weigert, Prog. Part. Nucl. Phys. **55**, 461 (2005); F. Gelis, R. Venugopalan, Acta Phys. Polon. **B 37**, 3253 (2006);
  10. F. Gelis, T. Lappi, R. Venugopalan, Int. J. Mod. Phys. E **16**, 2595 (2007).
  11. L.D. McLerran, R. Venugopalan, Phys. Rev. **D 49**, 2233 (1994); *ibid.* 3352 (1994); *ibid.* **50**, 2225 (1994).
  12. I. Balitsky, Nucl. Phys. **B 463**, 99 (1996).
  13. Yu.V. Kovchegov, Phys. Rev. **D 61**, 074018 (2000).
  14. J. Jalilian-Marian, A. Kovner, A. Leonidov, H. Weigert, Nucl. Phys. **B 504**, 415 (1997); *ibid.* Phys. Rev. **D 59**, 014014 (1999); *ibid.* 034007 (1999), Erratum. *ibid.* 099903 (1999); J. Jalilian-Marian, A. Kovner, H. Weigert, Phys. Rev. **D 59**, 014015 (1999); A. Kovner, G. Milhano, H. Weigert, Phys. Rev. **D 62**, 114005 (2000); H. Weigert, Nucl. Phys. **A 703**, 823 (2002).
  15. E. Iancu, A. Leonidov, L.D. McLerran, Nucl. Phys. **A 692**, 583 (2001); *ibid.* Phys. Lett. **B 510**, 133 (2001); E. Ferreiro, E. Iancu, A. Leonidov, L.D. McLerran, Nucl. Phys. **A 703**, 489 (2002).
  16. E. Iancu, L.D. McLerran, Phys. Lett. **B 510**, 145 (2001).
  17. A.H. Mueller, Nucl. Phys. **B 643**, 501 (2002); E. Iancu, K. Itakura, L.D. McLerran, Nucl. Phys. **A 724**, 181 (2003).
  18. A.H. Mueller, Nucl. Phys. **B 558**, 285 (1999).

19. W. Van Saarloos, Phys. Rept. **386**, 29 (2003).
20. S. Munier, R. Peschanski, Phys. Rev. Lett. **91**, 232001 (2003); *ibid.* Phys. Rev. **D 69**, 034008 (2004).
21. E.M. Levin, K. Tuchin, Nucl. Phys. **B 573**, 833 (2000); *ibid.* Nucl. Phys. **A 691**, 779 (2001); *ibid.* **693**, 787 (2001); N. Armesto, M.A. Braun, Eur. Phys. J. **C 20**, 517 (2001); *ibid.* **22**, 351 (2001); E. Levin, M. Lublinsky, Nucl. Phys. **A 696**, 833 (2001); *ibid.* Phys. Lett. **B 521**, 233 (2001); M. Lublinsky, Eur. Phys. J. **C 21**, 513 (2001); K. Golec-Biernat, L. Motyka, A.M. Stasto, Phys. Rev. **D 65**, 074037 (2002).
22. K. Rummukainen, H. Weigert, Nucl. Phys. **A 739**, 183 (2004).
23. E. Iancu, K. Itakura, L.D. McLerran, Nucl. Phys. **A 708**, 327 (2002); A.H. Mueller, D.N. Triantafyllopoulos, Nucl. Phys. **B 640**, 331 (2002).
24. D.N. Triantafyllopoulos, Nucl. Phys. **B 648**, 293 (2003).
25. A.M. Stasto, K. Golec-Biernat, J. Kwiecinski, Phys. Rev. Lett. **86**, 596 (2001).
26. F. Gelis, R. Peschanski, L. Schoeffel, G. Soyez, Phys. Lett. **B.647**, 376 (2007).
27. F. Gelis, R. Venugopalan, Nucl. Phys. **A 776**, 135 (2006); *ibid.* **779**, 177 (2006).
28. Yu.V. Kovchegov, J. Kuokkanen, K. Rummukainen, H. Weigert, Nucl. Phys. **A 823**, 47 (2009).
29. J.P. Blaizot, E. Iancu, H. Weigert, Nucl. Phys. **A 713**, 441 (2003).
30. S. Jeon, R. Venugopalan, Phys. Rev. **D 70**, 105012 (2004).
31. S. Jeon, R. Venugopalan, Phys. Rev. **D 71**, 125003 (2005).
32. Y. Hatta, E. Iancu, K. Itakura, L. McLerran, Nucl. Phys. **A 760**, 172

- (2005); Yu.V. Kovchegov, L. Szymanowski, S. Wallon, Phys. Lett. **B 586**, 267 (2004).
33. L.D. McLerran, AIP Conf. Proc. **490**, 42 (1999).
34. A.H. Mueller, Nucl. Phys. **A 724**, 223 (2003).
35. E. Brunet, B. Derrida, A.H. Mueller, S. Munier, Europhys. Lett. **76**, 1 (2006); S. Munier, Phys. Rept. **473**, 1 (2009).
36. E. Brunet, B. Derrida, Phys. Rev. E **56**, 2597 (1997); *ibid.* Comp. Phys. Comm. **121-122**, 376 (1999); *ibid.* J. Stat. Phys. **103**, 269 (2001).
37. A.H. Mueller, A.I. Shoshi, Nucl. Phys. **B 692**, 175 (2004).
38. E. Iancu, A.H. Mueller, S. Munier, Phys. Lett. **B 606**, 342 (2005).
39. E. Iancu, D.T. Triantafyllopoulos, Nucl. Phys. **A 756**, 419 (2005); *ibid.* Phys. Lett. **B 610**, 253 (2005).
40. E. Iancu, J.T. de Santana Amaral, G. Soyez, D.N. Triantafyllopoulos, Nucl. Phys. **A 786**, 131 (2007).
41. A.H. Mueller, A.I. Shoshi, S.M.H. Wong, Nucl. Phys. **B 715**, 440 (2005).
42. A. Kovner, M. Lublinsky, Phys. Rev. **D 71**, 085004 (2005); *ibid.* Phys. Rev. Lett. **94**, 181603 (2005); Y. Hatta, E. Iancu, L. McLerran, A. Stasto, D.N. Triantafyllopoulos, Nucl. Phys. **A 764**, 423 (2006); I. Balitsky, Phys. Rev. **D 72**, 074027 (2005).
43. A. Dumitru, E. Iancu, L. Portugal, G. Soyez, D.N. Triantafyllopoulos, JHEP **0708**, 062 (2007).
44. I. Balitsky, Phys. Rev. **D 75**, 014001 (2007); I. Balitsky, G.A. Chirilli, Phys. Rev. **D 77**, 014019 (2008); E. Gardi, J. Kuokkanen, K. Rummukainen, H. Weigert, Nucl. Phys. **A 784**, 282 (2007); Yu.V. Kovchegov, H. Weigert, Nucl. Phys. **A 784**, 188 (2007).

45. J.L. Albacete, N. Armesto, J.G. Milhano, C.A. Salgado, Phys. Rev. **D 80**, 034031 (2009).
46. V.N. Gribov, B.L. Ioffe, I.Y. Pomeranchuk, Sov. J. Nucl. Phys. **2**, 549 (1966); B.L. Ioffe, Phys. Lett. **B 30**, 123 (1969).
47. N.N. Nikolaev, B.G. Zakharov, Phys. Lett. **B 332**, 184 (1994).
48. L.D. McLerran, R. Venugopalan, Phys. Rev. **D 59**, 094002 (1999).
49. R. Venugopalan, Acta Phys. Polon. **B 30**, 3731 (1999).
50. F. Gelis, J. Jalilian-Marian, Phys. Rev. **D 66**, 014021 (2002); *ibid.* 094014, (2002); *ibid.* **76**, 074015 (2007); J. Jalilian-Marian, Eur. Phys. J **C 61**, 789 (2009); B.Z. Kopeliovich, J. Raufeisen, A.V. Tarasov, M.B. Johnson, Phys. Rev. **C 67**, 014903 (2003).
51. J.C. Collins, R.K. Ellis, Nucl. Phys. **B 360**, 3 (1991); S. Catani, M. Ciafaloni, F. Hautmann, Nucl. Phys. **B 366**, 135 (1991); E.M. Levin, M.G. Ryskin, Yu. M. Shabelsky, A.G. Shuvaev, Sov. J. Nucl. Phys. **53**, 657 (1991).
52. Yu.V. Kovchegov, A.H. Mueller, Nucl. Phys. **B 529**, 451 (1998).
53. A. Dumitru, L.D. McLerran, Nucl. Phys. **A 700**, 492 (2002).
54. F. Gelis, R. Venugopalan, Phys. Rev. **D 69**, 014019 (2004).
55. A. Krasnitz, R. Venugopalan, Phys. Rev. Lett. **86**, 1717 (2001).
56. J.P. Blaizot, F. Gelis, R. Venugopalan, Nucl. Phys. **A 743**, 57 (2004).
57. N.N. Nikolaev, W. Schafer, B.G. Zakharov, Phys. Rev. Lett. **95**, 221803 (2005).
58. F. Gelis, T. Lappi, R. Venugopalan, Phys. Rev. **D 78**, 054019 (2008); *ibid.* 054020 (2008); *ibid.* **79**, 094017 (2009).
59. A. Krasnitz, R. Venugopalan, Nucl. Phys. **B 557**, 237 (1999); *ibid.* Phys. Rev. Lett. **84**, 4309 (2000); A. Krasnitz, Y. Nara, R. Venugopalan, Phys.

- Rev. Lett. **87**, 192302 (2001).
60. A. Krasnitz, Y. Nara, R. Venugopalan, Nucl. Phys. **A 727**, 427 (2003).
61. T. Lappi, Phys. Rev. **C 67**, 054903 (2003); *ibid.* Phys. Lett. **B 643**, 11 (2006).
62. A. Krasnitz, Y. Nara, R. Venugopalan, Phys. Lett. **B 554**, 21 (2003); *ibid.* Nucl. Phys. **A 717**, 268 (2003); T. Lappi, R. Venugopalan, Phys. Rev. **C 74**, 054905 (2006).
63. T. Lappi, L.D. McLerran, Nucl. Phys. **A 772**, 200 (2006).
64. K. Dusling, F. Gelis, T. Lappi, R. Venugopalan, arXiv:0911.2720.
65. B. Alver, et al., [PHOBOS Collaboration] arXiv:0903.2811.
66. T. Lappi, S. Srednyak, R. Venugopalan, arXiv:0911.2068.
67. A. Dumitru, F. Gelis, L. McLerran, R. Venugopalan, Nucl. Phys. **A 810**, 91 (2008).
68. K. Dusling, D. Fernandez-Fraile, R. Venugopalan, Nucl. Phys. **A 828**, 161 (2009).
69. F. Gelis, T. Lappi, L. McLerran, Nucl. Phys. **A 828**, 149 (2009).
70. D. Kharzeev, A. Krasnitz, R. Venugopalan, Phys. Lett. **B 545**, 298 (2002).
71. D.E. Kharzeev, L.D. McLerran, H.J. Warringa, Nucl. Phys. **A 803**, 227 (2008).
72. H. Fujii, K. Itakura, Nucl. Phys. **A 809**, 88 (2008); H. Fujii, K. Itakura, A. Iwazaki, Nucl. Phys. **A 828**, 178 (2009); K. Fukushima, Phys. Rev. **C 75**, 021902 (2007); Erratum: arXiv:0711.2634; S. Mrowczynski, Acta Phys. Polon. **B 39**, 1665 (2008).
73. P. Romatschke, R. Venugopalan, Phys. Rev. Lett. **96**, 062302 (2006); *ibid.* Phys. Rev. **D 74**, 045011 (2006).

74. K. Fukushima, F. Gelis, L. McLerran, Nucl. Phys. **A 786**, 107 (2007).
75. Z. Xu, C. Greiner, Phys. Rev. **C 71**, 064901 (2005); F. Gelis, S. Jeon, R. Venugopalan, Nucl. Phys. **A 817**, 61 (2009).
76. B.B. Back, et al., [PHOBOS collaboration] Phys. Rev. Lett. **91**, 052303 (2003).
77. F. Gelis, A. Stasto, R. Venugopalan, Eur. Phys. J. **C 48**, 489 (2006).
78. C. Marquet, L. Schoeffel, Phys. Lett. **B 639**, 471 (2006).
79. E. Iancu, K. Itakura, S. Munier, Phys. Lett. **B 590**, 199 (2004).
80. G. Soyez, Phys. Lett. **B 655**, 32 (2007).
81. H. Kowalski, L. Motyka, G. Watt, Phys. Rev. **D 74**, 074016 (2006).
82. F. Caola, S. Forte, Phys. Rev. Lett. **101**, 022001 (2008).
83. K. Golec-Biernat, M. Wüsthoff, Phys. Rev. **D 59**, 014017 (1999); *ibid.* **60**, 114023 (1999).
84. J. Bartels, K. Golec-Biernat, H. Kowalski, Phys. Rev. **D 66**, 014001 (2002).
85. H. Kowalski, D. Teaney, Phys. Rev. **D 68**, 114005 (2003).
86. J.R. Forshaw, R. Sandapen, G. Shaw, Phys. Rev. **D 69**, 094013 (2004); *ibid.* Phys. Lett. **B 594**, 283 (2004); *ibid.* JHEP **0412**, 052 (2004); *ibid.* **0611**, 025 (2006).
87. F.E. Low, Phys. Rev. **D 12**, 163 (1975); S. Nussinov, Phys. Rev. Lett. **34**, 1286 (1975).
88. A. Caldwell, H. Kowalski, arXiv:0909.1254.
89. H. Kowalski, T. Lappi, C. Marquet, R. Venugopalan, Phys. Rev. **C 78**, 045201 (2008).
90. S. Munier, A.M. Stasto, A.H. Mueller, Nucl. Phys. **B 603**, 427 (2001); T. Rogers, V. Guzey, M. Strikman, X. Zu, Phys. Rev. **D 69**, 074011 (2004).

91. J.D. Bjorken, hep-ph/9601363.
92. A. Freund, K. Rummukainen, H. Weigert, A. Schafer, Phys. Rev. Lett. **90**, 222002 (2003); N. Armesto, C.A. Salgado, U.A. Wiedemann, Phys. Rev. Lett. **94**, 022002 (2005).
93. H. Kowalski, T. Lappi, R. Venugopalan, Phys. Rev. Lett. **100**, 022303 (2008).
94. M.S. Kugeratski, V.P. Goncalves, F.S. Navarra, Eur. Phys. J. **C 46**, 413 (2006).
95. C. Marquet, B.-W. Xiao, F. Yuan, Phys. Lett. **B 682**, 207 (2009).
96. V.P. Goncalves, M.S. Kugeratski, M.V.T. Machado, F.S. Navarra, Phys. Rev. **C 80**, 025202 (2009); F. Dominguez, C. Marquet, B. Wu, Nucl. Phys. **A 823**, 99 (2009).
97. M.V.T. Machado, arXiv:0905.4516.
98. J. Jalilian-Marian, Phys. Rev. **C 70**, 027902 (2004).
99. J.L. Albacete, Phys. Rev. Lett. **99**, 262301 (2007).
100. J.P. Blaizot, F. Gelis, R. Venugopalan, Nucl. Phys. **A 743**, 13 (2004).
101. D. Kharzeev, E. Levin, Phys. Lett. **B 523**, 79 (2001).
102. A.H. Mueller, Nucl. Phys. **B 572**, 227 (2000).
103. D. Kharzeev, M. Nardi, Phys. Lett. **B 507**, 121 (2001).
104. D. Kharzeev, E. Levin, M. Nardi, Nucl. Phys. **A 730**, 448 (2004).
105. A. Dumitru, J. Jalilian-Marian, Phys. Rev. Lett. **89**, 022301 (2002); *ibid.* Phys. Lett. **B 547**, 15 (2002).
106. F. Gelis, J. Jalilian-Marian, Phys. Rev. **D 67**, 074019 (2003).
107. A. Dumitru, A. Hayashigaki, J. Jalilian-Marian, Nucl. Phys. **A 765**, 464 (2006).

108. J.L. Albacete, C. Marquet, arXiv:1001.1378.
109. J.D. Bjorken, FERMILAB-PUB-82-059-THY (1982); X.N. Wang, M. Gyulassy, Phys. Rev. Lett. **68**, 1480 (1992); M. Gyulassy, X.N. Wang, Nucl. Phys. **B 420**, 583 (1994); R. Baier, Y.L. Dokshitzer, S. Peigné, D. Schiff, Phys. Lett. **B 345**, 277 (1995); R. Baier, Y.L. Dokshitzer, A.H. Mueller, S. Peigné, D. Schiff, Nucl. Phys. **B 483**, 291 (1997); M. Gyulassy, I. Vitev, X.N. Wang, B.N. Zhang, nucl-th/0302077.
110. D. Kharzeev, E. Levin, L.D. McLerran, Phys. Lett. **B 561**, 93 (2003); J.L. Albacete, N. Armesto, A. Kovner, C.A. Salgado, U.A. Wiedemann, Phys. Rev. Lett. **92**, 082001 (2004).
111. I. Arsene, et al., [BRAHMS collaboration] Phys. Rev. Lett. **93**, 242303 (2004).
112. J. Adams, et al., Phys. Rev. Lett. **97**, 152302 (2006).
113. E. Iancu, K. Itakura, D. Triantafyllopoulos, Nucl. Phys. **A 742**, 182 (2004).
114. D. Kharzeev, Yu. Kovchegov, K. Tuchin, Phys. Rev. **D 68**, 094013 (2003); *ibid.* Phys. Lett. **B 599**, 23 (2004).
115. V.P. Goncalves, M.S. Kugeratski, M.V.T. Machado, F.S. Navarra, Phys. Lett. **B 643**, 273 (2006).
116. J. Jalilian-Marian, Nucl. Phys. **A 770**, 210 (2006).
117. C. Marquet, Nucl. Phys. **A 796**, 41 (2007).
118. C. Marquet, talk at CATHIE-TECHQM workshop, BNL, Dec. 14th-18th, 2009; K. Tuchin, arXiv:0912.5479.
119. D. Kharzeev, E. Levin, L.D. McLerran, Nucl. Phys. **A 748**, 627 (2005); J.W. Qiu, I. Vitev, Phys. Lett. **B 632**, 507 (2006).
120. J. Adams, et al., [STAR Collaboration] Phys. Rev. Lett. **95**, 152301 (2005).



121. L. Molnar, *J. Phys. G* **34**, S593 (2007).
122. J. Adams, et al., [STAR Collaboration] *Phys. Rev. C* **73**, 064907 (2006).
123. B.I. Abelev, et al., [STAR Collaboration] arXiv:0909.0191.
124. M. Daugherty, [STAR Collaboration] *J. Phys. G* **35**, 104090 (2008).
125. P.K. Netrakanti, [STAR Collaboration] *J. Phys. G* **35**, 104010 (2008); B.I. Abelev, et al., [STAR Collaboration] *Phys. Rev. Lett.* **102**, 052302 (2009).
126. S.A. Voloshin, *Phys. Lett. B* **632**, 490 (2006); E.V. Shuryak, *Phys. Rev. C* **76**, 047901 (2007); C.A. Pruneau, S. Gavin, S.A. Voloshin, *Nucl. Phys. A* **802**, 107 (2008).
127. S. Gavin, L. McLerran, G. Moschelli, *Phys. Rev. C* **79**, 051902 (2009); G. Moschelli, S. Gavin, L.D. McLerran, *Eur. Phys. J. C* **62**, 277 (2009).
128. R. Andrade, F. Grassi, Y. Hama, W.L. Qian, arXiv:0912.0703; T. Osada, arXiv:0911.2303; J. Takahashi, B.M. Tavares, W.L. Qian, F. Grassi, Y. Hama, T. Kodama, N. Xu, arXiv:0902.4870.
129. A. Adare, et al., [PHENIX Collaboration] *Phys. Rev. C* **78**, 014901 (2008).
130. J. Chen, [PHENIX Collaboration] talk at the 26th Winter Workshop on Nuclear Dynamics, Ochos Rios, Jamaica, Jan. 2nd-9th, 2010.
131. J.L. Nagle, *Nucl. Phys. A* **830**, 147C (2009).
132. A.H. Mueller, H. Navelet, *Nucl. Phys. B* **282**, 727 (1987).
133. L. Alvero, J.C. Collins, J. Terron, J.J. Whitmore, *Phys. Rev. D* **59**, 074022 (1999).
134. A. Deshpande, R. Milner, R. Venugopalan, W. Vogelsang, *Ann. Rev. Nucl. Part. Sci.* **55**, 165 (2005); J.B. Dainton, M. Klein, P. Newman, E. Perez, F. Willeke, *JINST* **1**, P10001 (2006).